

## Article

# Industrial Heat Source-Related PM<sub>2.5</sub> Concentration Estimates and Analysis Using New Three-Stage Model in the Beijing–Tianjin–Hebei Region

Yi Zeng<sup>1</sup>, Xin Sui<sup>1,2</sup>, Caihong Ma<sup>2,\*</sup>, Ruilin Liao<sup>1,2</sup>, Jin Yang<sup>2</sup>, Dacheng Wang<sup>2</sup> and Pengyu Zhang<sup>1,2</sup>

<sup>1</sup> School of Information Science and Technology, Beijing Forestry University, Beijing 100083, China; zengyi@bjfu.edu.cn (Y.Z.); suixin09@bjfu.edu.cn (X.S.); liaoruilin1@bjfu.edu.cn (R.L.); blfuzpy@bjfu.edu.cn (P.Z.)

<sup>2</sup> Aerospace Information Research Institute, Chinese Academy of Sciences, Beijing 100094, China; yangjin@aircas.ac.cn (J.Y.); wangdc@aircas.ac.cn (D.W.)

\* Correspondence: mach@radi.ac.cn; Tel.: +86-152-1067-5780

**Abstract:** The prevalent high-energy, high-pollution and high-emission economic model has led to significant air pollution challenges in recent years. The industrial sector in the Beijing–Tianjin–Hebei (BTH) region is a notable source of atmospheric pollutants, with industrial heat sources (IHSs) being primary contributors to this pollution. Effectively managing emissions from these sources is pivotal for achieving air pollution control goals in the region. A new three-stage model using multi-source long-term data was proposed to estimate atmospheric, delicate particulate matter (PM<sub>2.5</sub>) concentrations caused by IHS. In the first stage, a region-growing algorithm was used to identify the IHS radiation areas. In the second and third stages, based on a seasonal trend decomposition procedure based on Loess (STL), multiple linear regression, and U-convLSTM models, IHS-related PM<sub>2.5</sub> concentrations caused by meteorological and anthropogenic conditions were removed using long-term data from 2012 to 2021. Finally, this study analyzed the spatial and temporal variations in IHS-related PM<sub>2.5</sub> concentrations in the BTH region. The findings reveal that PM<sub>2.5</sub> concentrations in IHS radiation areas were higher than in background areas, with approximately 33.16% attributable to IHS activities. A decreasing trend in IHS-related PM<sub>2.5</sub> concentrations was observed. Seasonal and spatial analyses indicated higher concentrations in the industrially dense southern region, particularly during autumn and winter. Moreover, a case study in Handan's She County demonstrated dynamic fluctuations in IHS-related PM<sub>2.5</sub> concentrations, with notable reductions during periods of industrial inactivity. Our results aligned closely with previous studies and actual IHS operations, showing strong positive correlations with related industrial indices. This study's outcomes are theoretically and practically significant for understanding and addressing the regional air quality caused by IHSs, contributing positively to regional environmental quality improvement and sustainable industrial development.

**Keywords:** PM<sub>2.5</sub>; industry heat sources radiation areas; Beijing–Tianjin–Hebei



**Citation:** Zeng, Y.; Sui, X.; Ma, C.; Liao, R.; Yang, J.; Wang, D.; Zhang, P. Industrial Heat Source-Related PM<sub>2.5</sub> Concentration Estimates and Analysis Using New Three-Stage Model in the Beijing–Tianjin–Hebei Region. *Atmosphere* **2024**, *15*, 131. <https://doi.org/10.3390/atmos15010131>

Academic Editors: Enrico Ferrero and Elvira Kovač-Andrić

Received: 24 December 2023

Revised: 11 January 2024

Accepted: 15 January 2024

Published: 20 January 2024



**Copyright:** © 2024 by the authors. Licensee MDPI, Basel, Switzerland. This article is an open access article distributed under the terms and conditions of the Creative Commons Attribution (CC BY) license (<https://creativecommons.org/licenses/by/4.0/>).

## 1. Introduction

Particulate matter with a diameter of 2.5 μm or less, commonly called PM<sub>2.5</sub>, has significant adverse effects on the atmospheric environment, climate change, and human health [1–3]. Industrial emissions from industrial heat sources (IHS) have been identified as one of the primary contributors to regional air pollution [4]. Moreover, these emissions' distribution and transformation processes profoundly impact the spatial and temporal variations in PM<sub>2.5</sub> concentrations [5,6]. Data show that the intensity of industrial pollution emissions in North China with dense IHSs is four times the national average, with atmospheric pollutant concentrations still exceeding the national average [7,8]. Therefore,

accurately estimating and analyzing the spatial and temporal variations in PM<sub>2.5</sub> concentrations caused by IHSs is crucial for optimizing emission control policies and combating air pollution.

Fuel consumption during industrial production causes many PM<sub>2.5</sub> emissions [9]. Estimating the contribution of industrial emissions to PM<sub>2.5</sub> requires complex and time-consuming emission source-apportionment studies [10]. Within the last few decades, significant efforts have been made by researchers to quantify the impact of industry on PM<sub>2.5</sub> concentrations, including emission inventories [11,12], source apportionment [13,14], and numerical models [15,16], as well as statistical models [17,18]. Many studies have predominantly aggregated industrial emission sources at a regional level, thereby assessing their collective impact on air quality [19,20]. This approach is grounded in analyzing emission inventories and the statistical data delineated in annual reports. Duan et al. quantified the contribution rates of the iron and steel industry to PM<sub>2.5</sub> emissions in the BTH region based on the emission inventory specific to this sector, primarily utilizing data derived from field measurements and emission factors [21]. Analogously, An et al. estimated the contribution of industrial sectors to PM<sub>2.5</sub> emissions in the Yangtze River Delta, utilizing an updated pollutant emission inventory and local measurement data [22]. However, these studies have relied on large-scale data for the spatial distribution of emissions and need help to locate emission sources accurately [23]. Source apportionment and numerical simulation methods elucidate the physical mechanisms behind pollutant formation and transport. These methodologies facilitate a nuanced assessment of PM<sub>2.5</sub> concentration contributions by various industries [24,25]. Dong et al. utilized the positive matrix factorization (PMF) model to intricately dissect the origins of PM<sub>2.5</sub> in Changchun, primarily employing data from air quality monitoring stations [26]. Their analysis revealed that secondary sources are the principal contributors to the city's PM<sub>2.5</sub> concentrations. Liu et al. employed the CAMx-PSAT model to assess the seasonal variations and sources of PM<sub>2.5</sub> in Beijing, identifying the industrial sector as one of the primary sources of PM<sub>2.5</sub> concentrations [27]. However, such models have required extensive a priori knowledge and intricate parameterization. Furthermore, these models need more generalizability, making them difficult to extend [28].

Statistical models bypass the intricate atmospheric physical and chemical processes, focusing instead on analyzing pollutant concentrations based on the data's inherent features [29]. Yuen conducted an analysis of the relationships between air quality and weather conditions using multiple regression techniques [30]. Ding et al. applied the seasonal-trend decomposition procedure based on Loess (STL) method to isolate meteorological fluctuations, subsequently positing that changes in ozone levels in Tianjin are largely driven by variations in precursor emissions [31]. However, traditional regression methods must be revised to address high-dimensional and nonlinear data, consequently constraining their performance. Therefore, these methods are frequently integrated with other models to enhance analytical capabilities [32]. The advancement of deep learning has provided a novel perspective for monitoring and decomposing PM<sub>2.5</sub> concentrations. Deep learning methods, which integrate non-linear patterns and network models, outperform simple statistical models regarding fitting accuracy [33]. Among various neural networks, long short-term memory (LSTM) networks, with their unique gate structures, have shown superiority in predicting time-series data [34]. Concurrently, as popular deep learning models, convolutional neural networks (CNN) effectively extract spatial features from data [35]. Therefore, some researchers have attempted to combine CNN with LSTM to study PM<sub>2.5</sub> concentrations from both temporal and spatial dimensions. Huang et al. proposed an APNet algorithm based on CNN-LSTM for predicting PM<sub>2.5</sub> concentrations in the upcoming hour, primarily utilizing data from air quality monitoring stations [36]. Xu et al. developed a weight-sharing deep learning framework and multi-objective optimization network based on the CNN-LSTM model to predict PM<sub>2.5</sub> concentrations in Xi'an [33]. The down-sampling structure in the U-Net model strengthens the extraction of spatial information, and its integration with CNN-LSTM has been shown to improve PM<sub>2.5</sub> forecasting

accuracy [37]. Ma et al. applied the U-ConvLSTM model to predict the long-term spatial distribution of PM<sub>2.5</sub>, effectively enhancing the precision of their predictions [38]. While previous studies have demonstrated strengths in predicting PM<sub>2.5</sub> concentrations, research on deep learning-based analysis of industrial impact on air quality indicators still needs to be completed. Accurately estimating PM<sub>2.5</sub> concentrations from IHSs over a long time series continues to present challenges.

This study aims to improve the limitations of low spatial and temporal resolution, data acquisition difficulties, and high modeling complexity in existing assessment methods. Therefore, multi-source ten-year daily long time series data were adopted to estimate the PM<sub>2.5</sub> concentrations from IHS-related PM<sub>2.5</sub> concentrations (IHS) in this study. The employed Comprehensive High-Resolution Air Pollution (CHAP) dataset is known for its high-resolution and comprehensive coverage, providing robust and accurate data crucial for our analysis [39–41]. Then, a three-stage model was proposed based on region-growing, STL, multiple regression methods, and U-ConvLSTM algorithms. In the first stage, a region-growing algorithm was used to identify the IHS radiation areas. In the second stage, STL and multiple regression methods were employed to eliminate the influence of meteorological conditions. In the third stage, the U-ConvLSTM model was finally utilized to extract the spatial and temporal features of PM<sub>2.5</sub> concentrations caused by other anthropogenic factors. It is pertinent to acknowledge the inherent uncertainties in this research, including potential biases in source data quality and limitations in analytical methods, as well as specific uncertainties in the CHAP and ERA5 datasets used. Finally, this study analyzed the spatial and temporal variations in IHS-related PM<sub>2.5</sub> concentrations in the BTH region, covering the period from 2012 to 2021. This analysis was performed from both a regional perspective and through the lens of individual IHS contributions. The results estimate air pollution caused by IHSs and provide scientific and technical support for formulating environmental protection policy and industrial layout.

## 2. Materials and Methods

### 2.1. Study Area

The BTH region (36.0°N–42.6° N, 113.5°E–119.8° E) is situated on the North China Plain (Figure 1), encompassing Beijing, Tianjin, and Hebei province [42]. The former two are municipalities, and Hebei Province comprises 11 prefecture-level cities. The Yan and Taihang mountain ranges in the north form a semi-enclosed structure around the region, resulting in low wind speeds and increased atmospheric stability. The BTH region hosts over 8% of China's population and is pivotal in driving economic growth in northern China [43]. Additionally, this region stands as the most extensive energy industrial base and a significant steel hub in China. The region's complex topographical and adverse meteorological conditions accentuate severe atmospheric pollution caused by substantial energy consumption emissions. In 2022, the annual average PM<sub>2.5</sub> concentration in the BTH and surrounding areas was 44 µg/m<sup>3</sup>, exceeding the national average by 16 µg/m<sup>3</sup>. This persistent environmental issue has sustained attention from government entities, the media, and various societal sectors [44].

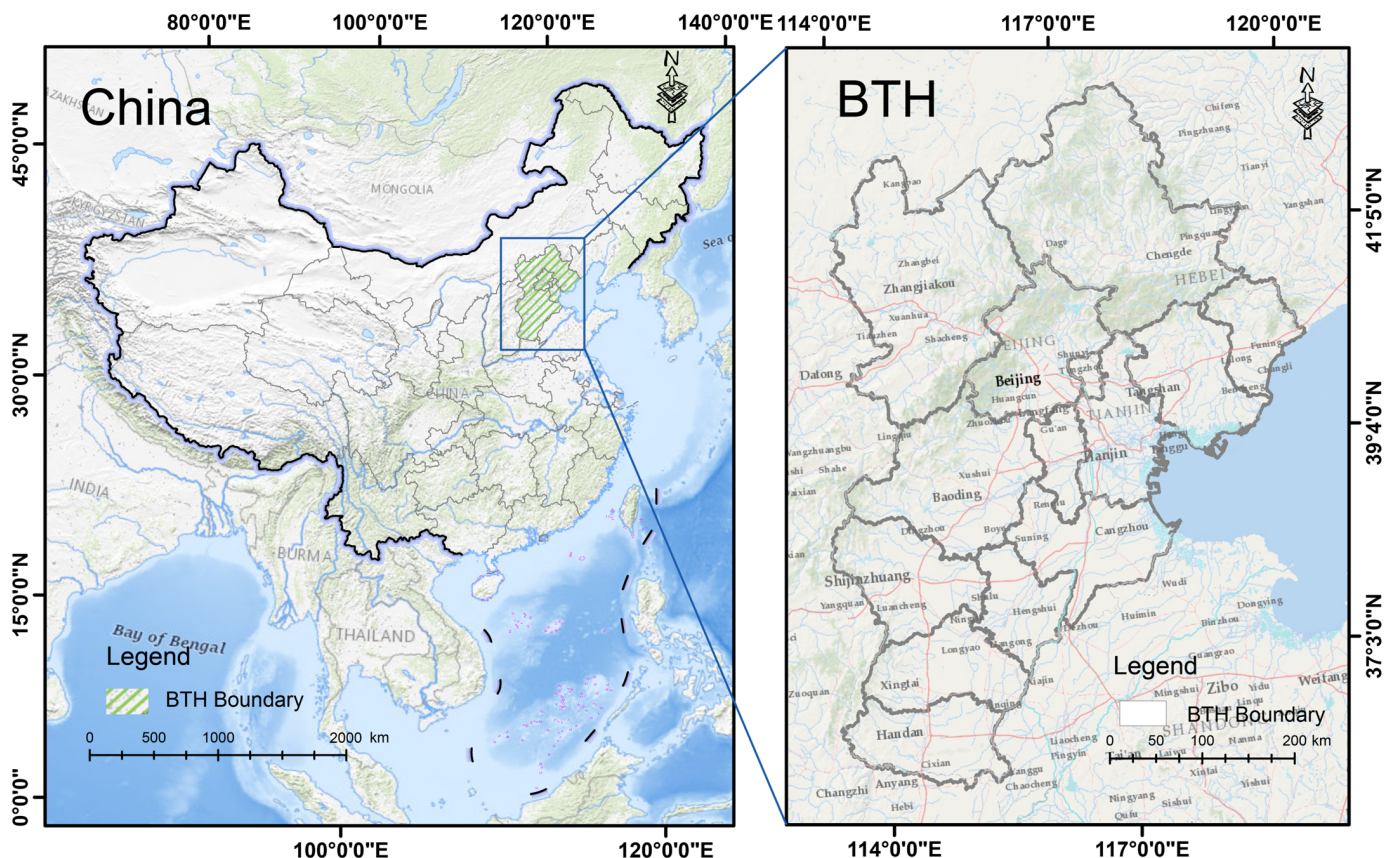


Figure 1. Study area.

2.2. Data Source

The data required for this study encompass PM<sub>2.5</sub> concentration data, natural geographic data, and socio-economic data. More information on the data can be seen in Table 1.

Table 1. Data description used in this study.

No.	Factors	Code	Datasets	Period	Space Resolution	Time Resolution	Data Source
1	ChinaHighPM <sub>2.5</sub> concentration	PM <sub>2.5</sub>	Comprehensive High-Resolution Air Pollution	2012–2021	1 km	1-day	National Tibetan Plateau/Third Pole Environment Data Center ( <a href="https://doi.org/10.5281/zenodo.3539349">https://doi.org/10.5281/zenodo.3539349</a> , accessed on 30 June 2023.)
2	2 m Air Temperature	T2M	ERA5	2012–2021	0.1° × 0.1°	1-day	Google Earth Engine ( <a href="https://earthengine.google.com/">https://earthengine.google.com/</a> , accessed on 30 June 2023.)
3	Total Precipitation	TP	ERA5	2012–2021	0.1° × 0.1°	1-day	Google Earth Engine ( <a href="https://earthengine.google.com/">https://earthengine.google.com/</a> , accessed on 30 June 2023.)
4	Surface Pressure	SP	ERA5	2012–2021	0.1° × 0.1°	1-day	Google Earth Engine ( <a href="https://earthengine.google.com/">https://earthengine.google.com/</a> , accessed on 30 June 2023.)
5	10 m U Wind Component	10U	ERA5	2012–2021	0.1° × 0.1°	1-day	Google Earth Engine ( <a href="https://earthengine.google.com/">https://earthengine.google.com/</a> , accessed on 30 June 2023.)

Table 1. Cont.

No.	Factors	Code	Datasets	Period	Space Resolution	Time Resolution	Data Source
6	10 m V Wind Component	10V	ERA5	2012–2021	0.1° × 0.1°	1-day	Google Earth Engine ( <a href="https://earthengine.google.com/">https://earthengine.google.com/</a> ), accessed on 30 June 2023.)
7	Relative Humidity	RH	ERA5	2012–2021	0.1° × 0.1°	1-day	Google Earth Engine ( <a href="https://earthengine.google.com/">https://earthengine.google.com/</a> ), accessed on 30 June 2023.)
8	Copernicus DEM	DEM	ESA	2015	30 m × 30 m	1-year	ESA ( <a href="https://panda.copernicus.eu/">https://panda.copernicus.eu/</a> ), accessed on 30 June 2023.)
9	Industrial Heat Sources	IHS	A dataset of in-operation industrial heat source objects in BTH	2012–2021	375 m	1-year	Science Data Bank ( <a href="https://doi.org/10.57760/sciencedb.j00001.00430">https://doi.org/10.57760/sciencedb.j00001.00430</a> ), accessed on 30 June 2023.)
10	Carbon Emissions	CE	CCG	2015, 2020	City	1-year	China City Greenhouse Gas Working Group ( <a href="http://www.cityghg.com/toCauses?id=4">http://www.cityghg.com/toCauses?id=4</a> ), accessed on 30 June 2023.)
11	Industrial Indices	II	Statistical yearbooks of Beijing, Tianjin and Hebei provinces	2012–2021	Province	1-year	City Data Query Platform ( <a href="https://www.gotohui.com/">https://www.gotohui.com/</a> ), accessed on 30 June 2023.)
12	Environmental Emissions	EE	Statistical yearbooks of Beijing, Tianjin and Hebei provinces	2012–2021	Province	1-year	City Data Query Platform ( <a href="https://www.gotohui.com/">https://www.gotohui.com/</a> ), accessed on 30 June 2023.)
13	Raw Material Production	RP	Statistical yearbooks of Beijing, Tianjin and Hebei provinces	2012–2021	Province	1-year	City Data Query Platform ( <a href="https://www.gotohui.com/">https://www.gotohui.com/</a> ), accessed on 30 June 2023.)

### 2.2.1. PM<sub>2.5</sub> Concentration Data

The PM<sub>2.5</sub> concentration dataset was derived from the CHAP dataset (available at <https://weijing-rs.github.io/product.html>, accessed on 30 June 2023). The CHAP dataset is known for its encapsulation of long-term, full-coverage, high-resolution, and high-quality data on ground-level air pollutants within China [39–41]. Many significant data sources, including ground-based measurements, satellite remote sensing products, atmospheric reanalysis, and model simulations, were incorporated to generate the dataset. It boasted a temporal resolution of one day and a spatial resolution of one kilometer. Additionally, the daily PM<sub>2.5</sub> estimates exhibit high accuracy, evidenced by an average cross-validation coefficient of determination of 0.92. Daily PM<sub>2.5</sub> data spanning from 2012 to 2021 were employed as the primary data source in this study. The focus was exploring the spatial and temporal trends of PM<sub>2.5</sub> concentrations in the BTH regions.

### 2.2.2. Natural Geographic Data

Meteorological data were obtained from the ECMWF Reanalysis v5 (ERA5) dataset, the fifth-generation atmospheric reanalysis product of global climate produced by the European Centre for Medium-Range Weather Forecasts (ECMWF) (available at <https://earthengine.google.com/>, accessed on 30 June 2023). Compared to its predecessor, the ERA-Interim, ERA5 provided atmospheric analysis data with superior temporal and spatial resolutions [45]. The ERA5 DAILY data, downloaded from the Google Earth Engine (GEE) platform, comprised a temporal resolution of one day and a spatial resolution of 0.1° × 0.1°. This study extended the dataset period from 1 January 2012 to 31 December 2021.

The following parameters were selected to correlate meteorological variables with PM<sub>2.5</sub> concentrations: 2 m air temperature (T2M), total precipitation (TP), surface pressure (SP), 10 m u wind component (10U), and 10 m v wind component (10V). Relative humidity (RH) was then calculated using the t2m and 2 m dew point temperature. These six variables were crucial in isolating meteorological factors from PM<sub>2.5</sub> concentrations [46].

The digital elevation model (DEM) data were sourced from the Copernicus DEM, a product derived from global radar satellite observations (available at <https://panda.copernicus.eu/panda>, accessed on 30 June 2023) [47]. These observations were processed through interferometric techniques to yield the TanDEM-X DEM product. Subsequently, a semi-automated editing and sampling process was employed to refine this data into a 30 m grid, resulting in the Copernicus 30 m resolution DEM dataset.

### 2.2.3. Socio-Economic Data

The dataset for IHS was derived from research conducted by Ma et al. (available at <https://doi.org/10.57760/sciencedb.j00001.00430>, accessed on 30 June 2023) [48]. The k-means method was employed to identify heat source objects generated through the fire points' spatial density segmentation. Subsequently, a random forest algorithm was employed to identify and analyze IHSs. The results were validated and revised using Google Earth, other high-resolution satellite imagery, points of interest (POI) information, and field surveys. This process culminated in identifying 474 IHSs in the BTH region from 2012 to 2021. Furthermore, the dataset included attribute information on the operational status of the IHS, providing a precise reference for constructing the radiation area of the IHS.

The carbon emissions dataset was sourced from the China City Greenhouse Gas Working Group (CCG) (available at <http://www.cityghg.com/toCauses?id=4>, accessed on 30 June 2023). Drawing from internationally established and widely applied urban CO<sub>2</sub> emissions accounting methods and considering China's urban realities, the CCG calculated all direct and indirect emissions from cities purchasing electricity outside their administrative boundaries. Industrial indices, environmental emissions, and raw material production were sourced from the statistical yearbooks of Beijing, Tianjin, and Hebei provinces (available at <https://www.gotohui.com>, accessed on 30 June 2023). For this study, data from 2012 to 2021 were selected as key factors for measuring the correlation between IHS-related PM<sub>2.5</sub> concentrations and these indices.

### 2.3. Method

The technical route of this study is illustrated in Figure 2. This study proposed a new three-stage model using multi-source long-term data to estimate IHS-related PM<sub>2.5</sub> concentrations. In the first stage, the IHS radiation areas were established based on a region-growing algorithm using IHS and DEM data to identify the IHS radiation areas. In the second stage, pixel-by-pixel STL decomposition and multiple linear regression methods were employed to eliminate the influence of meteorological conditions. In the third stage, the U-ConvLSTM model was adopted to extract the background concentrations within the IHS radiation areas, thereby removing interference from other anthropogenic factors. Finally, the concentration and contribution of IHS-related PM<sub>2.5</sub> in the BTH Region were analyzed in three parts: the entire study area, all IHS radiation areas, and the typical individual IHS radiation area. The detailed steps of this procedure will be elaborated on in the following sections.

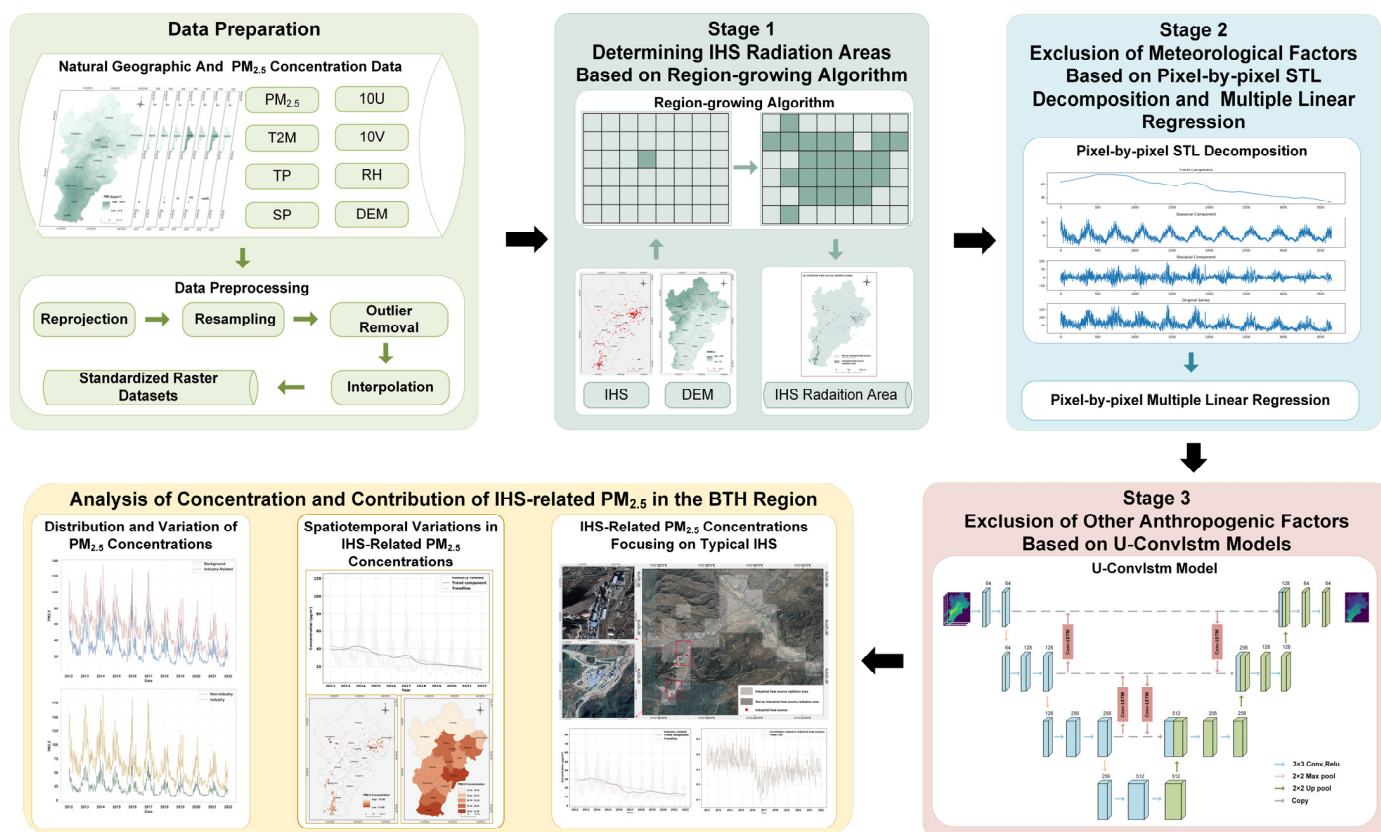


**Figure 2.** Technology route of IHS-related PM<sub>2.5</sub> concentration estimates and analyses in the BTH region using a three-stage model.

### 2.3.1. Data Preparation

PM<sub>2.5</sub> concentration data and meteorological data were transformed to the WGS\_1984 projection coordinate system in this study. Subsequently, the target area data were clipped based on the administrative boundaries of the BTH region. Due to variations in data sources, the temporal resolution of all datasets was harmonized to a daily scale, while the spatial resolution was consistently set to 1 km × 1 km. To ensure the integrity and reliability of the PM<sub>2.5</sub> data, outliers and missing values were systematically excluded. Anomalies within the data were identified and removed using a quartile-based method. Lastly, the Kriging interpolation technique was employed to fill in the gaps in PM<sub>2.5</sub> concentration and meteorological datasets.

### 2.3.2. Stage 1: Determining IHS Radiation Areas Based on Region-Growing Algorithm Using IHS and DEM Data

The IHS dataset provides spatial and temporal distributions of IHS [49]. Emissions and pollution from these sources impact not just the site but also the surrounding areas [50]. The region-growing algorithm using IHS and DEM data was implemented to define the IHS radiation areas [51]. The detailed steps of the region-growing method are as follows:

- (1) The IHS data were transformed from vector to raster format. The DEM and IHS data were resampled to align with the PM<sub>2.5</sub> concentration grid as a reference layer.
- (2) The region-growing algorithm was initiated from the central grid representing the IHSs, identified in Figure 3b. This grid's elevation was compared with the surrounding eight pixels. If the adjacent pixels displayed lower elevations, they were amalgamated into the IHS grid.
- (3) Repeat step (2) with all newly added grids serving as new growth points. The process persisted until either no lower elevation grids were identified or the predefined maximum impact distance was reached; at this point, the expansion ceased. Consequently,

all incorporated grids were classified as the IHS radiation areas. The maximum distance for each IHS pollution impact was set to 10 km, according to the recommended method for the risk assessment of environmental emergencies in administrative regions (Figure 3c) [52].

- (4) Replicating steps 2 and 3 was repeated to delineate all IHS radiation areas of each IHSs, as shown in Figure 3a.

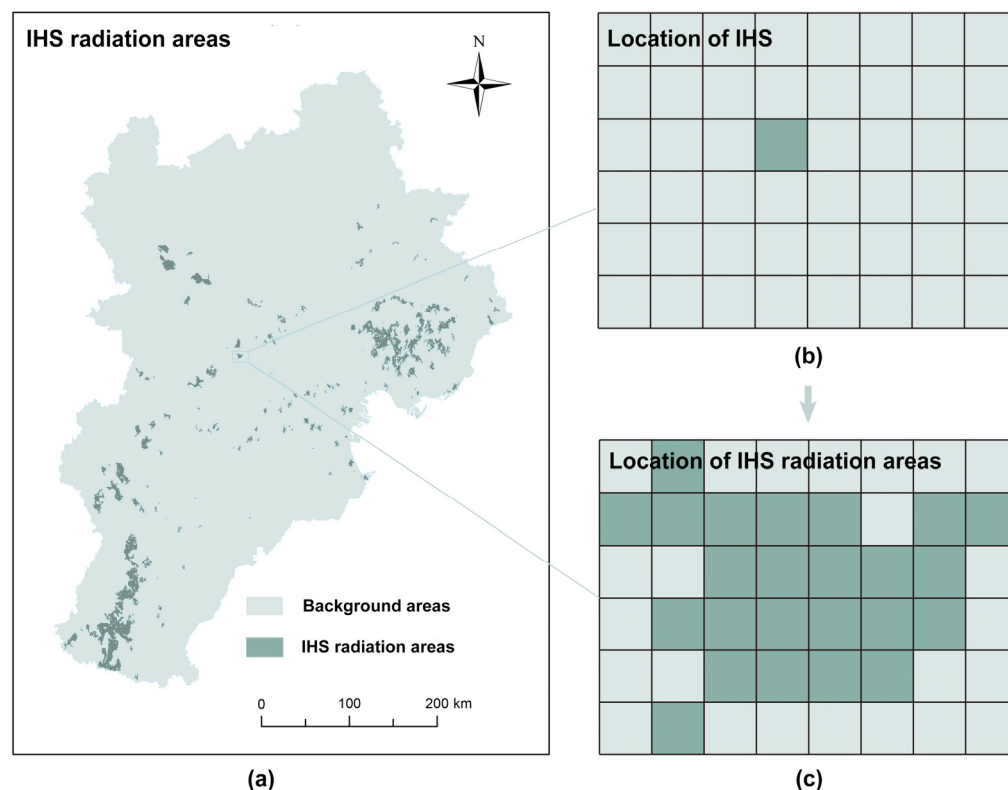


**Figure 3.** IHS radiation areas in the BTH region. (a) IHS radiation areas. (b) Location of IHSs. (c) Location of IHS radiation areas.

### 2.3.3. Stage 2: Exclusion of Meteorological Factors Based on Pixel-by-Pixel STL Decomposition and Multiple Linear Regression

The relationship between meteorological elements and air quality exhibits regional variability attributable to the distinct topographical features and climatic conditions. To objectively estimate the impact of IHSs on  $PM_{2.5}$  concentrations, it is necessary to exclude the influence of meteorological factors on the short-term and long-term variation in pollutant concentrations. This study used STL decomposition to remove the components influenced by short-term meteorological changes. Concurrently, a multiple linear regression approach was employed to negate the influence of long-term meteorological conditions on the  $PM_{2.5}$  concentration series. The specific process of elimination is depicted in Figure 4 (using the value of a single pixel as an example). The specific steps are as follows:

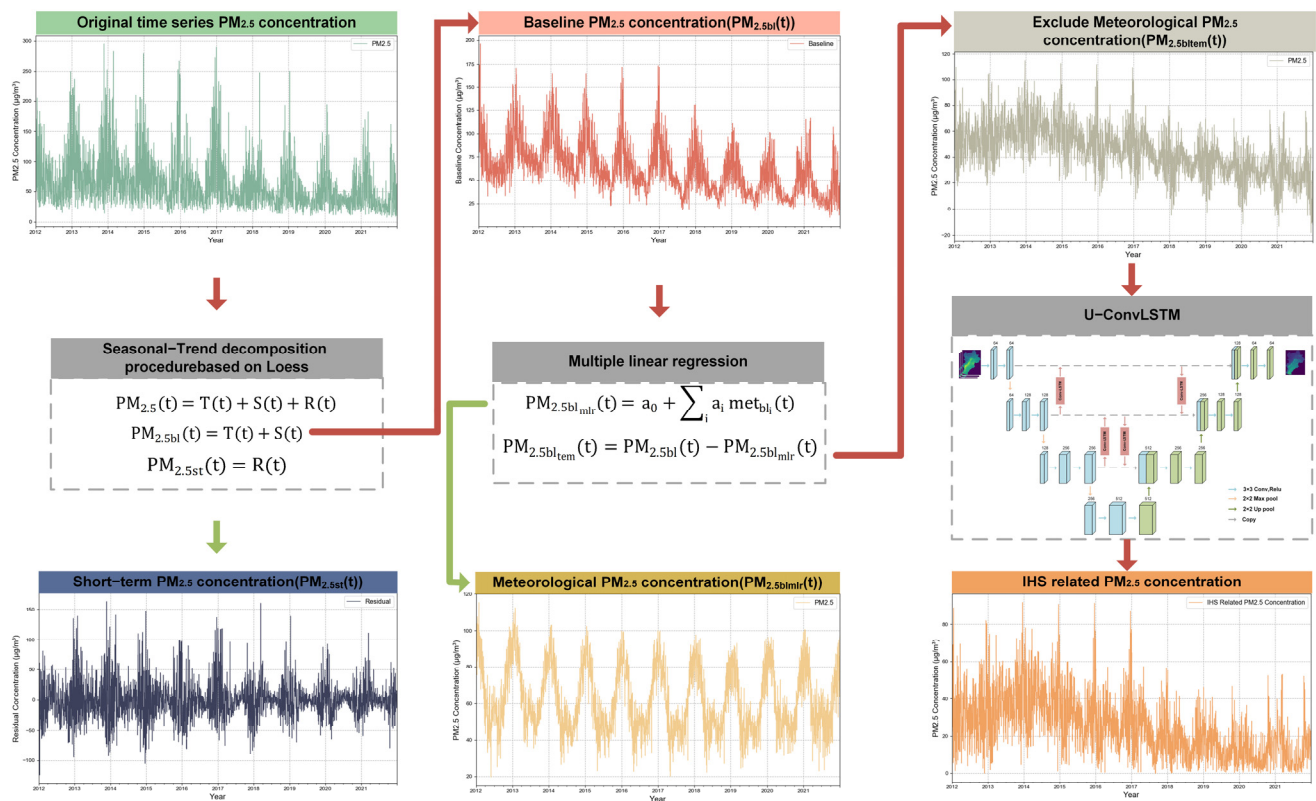


**Figure 4.** Process of meteorological and anthropogenic influence removal for estimating IHS impact on PM<sub>2.5</sub> concentrations (illustrated using a single pix value).

1. Exclusion of Short-term Meteorological Factors Based on STL Decomposition

STL decomposition is a non-parametric statistical method that consists of an inner loop for fitting trend and seasonal components and an outer loop for calculating robustness weights to reduce the impact of outliers [53]. Compared to other time-series decomposition methods, it offers greater precision and configurability. STL decomposition was utilized to separate the PM<sub>2.5</sub> concentration of each grid pixel into short-term, seasonal, and long-term components while excluding short-term fluctuations present in the original data. The short-term component is primarily influenced by short-term meteorological changes and, to a lesser extent, by short-term variations in pollutant emissions [54]. Seasonal and long-term components are mainly attributed to changes in human activity-related emissions of air pollutants and the seasonality and inter-annual variations in meteorological conditions. For the STL decomposition applied to our daily PM<sub>2.5</sub> concentration dataset spanning from 2012 to 2021, the seasonal window was set to 365 days, aiming to accurately capture the annual fluctuation patterns of PM<sub>2.5</sub> concentrations. After decomposition, the expression for the composition of atmospheric acceptable particulate matter concentrations for each pixel can be calculated as follows:

$$PM_{2.5}(t) = T(t) + S(t) + R(t), t = 1, 2, \dots, N \tag{1}$$

where PM<sub>2.5</sub>(t), T(t), S(t), and R(t) represent the observed values of atmospheric particulate matter concentration series, long-term fluctuation, seasonal fluctuation, and short-term fluctuation at time t, respectively, and N denotes the time series length.

The baseline concentration, obtained by excluding the short-term component, can be expressed as:

$$PM_{2.5bl}(t) = T(t) + S(t), t = 1, 2, \dots, N \tag{2}$$

where  $PM_{2.5bl}(t)$ ,  $T(t)$  and  $S(t)$  represent the baseline concentration of atmospheric particulate matter, long-term fluctuation, and seasonal fluctuation at time  $t$ , respectively, and  $N$  is the time series length.

## 2. Exclusion of Long-term Meteorological Factors Based on Multiple linear regression

$PM_{2.5bl}(t)$  is typically associated with long-term variations in meteorological conditions and emission sources. The research has indicated that meteorological factors can account for 31.96% of  $PM_{2.5}$  concentration variations in the BTH region [55]. In particular, temperature and relative humidity have been found to exert the most significant influence on air quality in the area. At the same time, precipitation, wind direction, wind speed, and surface pressure also play a role to some extent. As a commonly used statistical method, multiple linear regression facilitates the quantitative elucidation of the relationship between meteorological variables and  $PM_{2.5}$  concentrations. This methodology effectively discerns the extent of meteorological factors' impact on air quality [56]. The advantage of multiple linear regression lies in accurately describing the relationships between variables by adjusting the coefficients of each independent variable. In this study, a multiple linear regression model was constructed to eliminate the influence of long-term meteorological conditions on the  $PM_{2.5}$  concentration series. The specific implementation steps of model construction and analysis are as follows:

The STL decomposition method was employed to break down the pre-processed meteorological parameters into long-term, seasonal, and short-term fluctuations. Short-term fluctuations caused by meteorological changes and human activities were excluded, thereby retaining the baseline components of each meteorological parameter.

Multiple linear regression was performed for each meteorological variable using the daily averages or cumulative values of all meteorological elements, expressed as:

$$PM_{2.5bl_{mlr}}(t) = a_0 + \sum_i a_i met_{bl_i}(t), t = 1, 2, \dots, N \quad (3)$$

where  $met_{bl_i}(t)$  ( $i \in [1, 6]$ ) represents the baseline component of meteorological variable  $i$  at  $t$ , with  $i = 1, 2, 3, 4, 5, 6$  corresponding to  $t2m$ ,  $tp$ ,  $sp$ ,  $10u$ ,  $10v$  and  $rh$ , respectively.  $a_i$  is the regression coefficient for the corresponding meteorological variable,  $a_0$  is the intercept, and  $N$  represents the length of the time series.

The impacts of seasonal and inter-annual variations in meteorological conditions on atmospheric fine particulate matter concentrations were eliminated. The expression is as follows:

$$PM_{2.5bl_{tem}}(t) = PM_{2.5bl}(t) - PM_{2.5bl_{mlr}}(t), t = 1, 2, \dots, N \quad (4)$$

where  $PM_{2.5bl_{tem}}(t)$  represents the concentration of  $PM_{2.5}$  at  $t$  after excluding meteorological factors.

### 2.3.4. Stage 3: Exclusion of Other Anthropogenic Factors Based on U-ConvLSTM Model

In this research, the U-ConvLSTM model was employed to extract the spatial and temporal features of  $PM_{2.5}$  concentrations influenced by other anthropogenic factors in background areas, aiming to predict the  $PM_{2.5}$  concentrations in IHS radiation areas affected by these same factors. The exclusion process is shown in Figure 5, and the specific architecture of the model is depicted in Figure 5. Combining CNN with LSTM, the ConvLSTM model enhances traditional LSTM by incorporating convolutional operations within its structure [57]. This innovation lets the model grasp the data's temporal associations and spatial details. Developed initially for precipitation forecasting, it has extensive application in meteorological predictions. In our study, the model effectively discerned and encoded the local spatiotemporal characteristics of particulate matter concentrations influenced by various non-meteorological factors. The essential equations related to ConvLSTM can be calculated as follows:

$$i_t = \sigma(W_{xi} * X_t + W_{hi} * H_{t-1} + W_{ci} \circ C_{t-1} + b_i) \quad (5)$$

$$f_t = \sigma(W_{xf} * X_t + W_{hf} * H_{t-1} + W_{cf} \circ C_{t-1} + b_f) \tag{6}$$

$$C_t = f_t \circ C_{t-1} + i_t \circ \tanh(W_{xc} * X_t + W_{hc} * H_{t-1} + b_c) \tag{7}$$

$$o_t = \sigma(W_{xo} * X_t + W_{ho} * H_{t-1} + W_{co} \circ C_t + b_o) \tag{8}$$

$$H_t = o_t \circ \tanh(C_t) \tag{9}$$

where  $i_t$  denotes the output of the input gate,  $f_t$  denotes the output of the forget gate,  $C_t$  represents the state of the cell at the current moment,  $o_t$  corresponds to the gate's output, and  $H_t$  denotes the predicted output of updating the current sequence index.

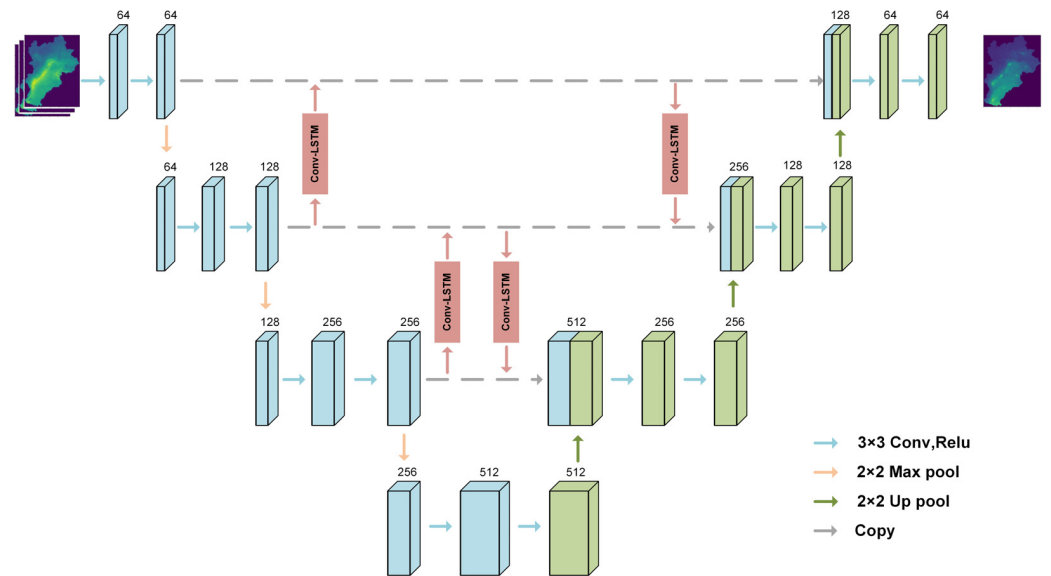


Figure 5. Structure of the U-convlstm model.

Furthermore, the encoder–decoder structure of the U-net maintained the spatial structure of images, facilitating the distinction and reconstruction of fine details in the data [38]. This feature is beneficial for identifying localized PM<sub>2.5</sub> concentration characteristics within background regions and precisely predicting PM<sub>2.5</sub> concentrations in IHS radiation areas influenced by other anthropogenic factors. The encoder comprised four layers, each incorporating a 3 × 3 convolution, 2 × 2 max pooling, and a ReLU activation function. Following downsampling, the encoder generated feature maps enriched with semantic information. The decoder then fused these acquired spatiotemporal features across various scales, employing upsampling and skip connections, ultimately producing the forecast through a 1 × 1 convolution. In this model, PM<sub>2.5bl<sub>tem</sub></sub> concentration images were inputted, with the PM<sub>2.5</sub> pixel concentrations in background areas considered to be influenced by anthropogenic factors. These data were the training set for predicting PM<sub>2.5</sub> concentrations in IHS radiation areas impacted by similar factors. Ultimately, the expression for IHS-related PM<sub>2.5</sub> concentrations was formulated as follows:

$$PM_{2.5ihs}(t) = PM_{2.5bl_{tem}}(t) - PM_{2.5bl_{oem}}(t), t = 1, 2, \dots, N \tag{10}$$

where PM<sub>2.5ihs</sub> represents the IHS-related PM<sub>2.5</sub> concentrations, PM<sub>2.5bl<sub>oem</sub></sub> represents the PM<sub>2.5</sub> concentrations influenced by other anthropogenic factors.

### 2.3.5. Statistical Analysis of IHS-Related PM<sub>2.5</sub> Concentrations

This research utilized various methods, such as the Mann–Whitney U test, correlation analysis, the Mann–Kendall test, and spatial autocorrelation analysis, to examine the spatiotemporal features and trends of IHS-related PM<sub>2.5</sub> concentrations in the study region. The methodologies are detailed below:

**Mann–Whitney U test:** A Mann–Whitney U test was conducted between the PM<sub>2.5</sub> concentrations in background areas and those in the IHS radiation areas to determine if IHS activities had a quantifiable impact on PM<sub>2.5</sub> levels. The Mann–Whitney U test, a non-parametric statistical method, compares the differences between two independent groups [58]. This test is beneficial when the data deviate from a normal distribution as a reliable substitute for the independent samples t-test. In this study, the Mann–Whitney U statistic can be computed as follows:

$$U = n_1 n_2 + \frac{n_1(n_1 + 1)}{2} - R_1 \quad (11)$$

where  $n_1$  and  $n_2$ , respectively, denote the sample sizes of the PM<sub>2.5</sub> concentration data from the background area and the IHS radiation area.  $R_1$  is the sum of the ranks for the background area. The lower the U statistic, the more substantial the evidence of a significant difference between the groups.

**Correlation analysis:** Correlation analysis is a statistical method used to assess the strength and direction of the linear relationship between two or more variables [59]. This study primarily employed correlation analysis to measure the association between IHS-related PM<sub>2.5</sub> concentrations and indicators such as the number of operational IHSs and carbon emissions. The correlation is quantified using Pearson’s correlation coefficient, which ranges from  $-1$  to  $+1$ . A coefficient value closer to  $1$  or  $-1$  indicates a stronger linear relationship between the variables. The Pearson correlation coefficient is calculated using the formula:

$$r = \frac{\sum(x_i - \bar{x})(y_i - \bar{y})}{\sqrt{\sum(x_i - \bar{x})^2 \sum(y_i - \bar{y})^2}} \quad (12)$$

where  $x_i$ ,  $y_i$  represent the observed values of IHS-related PM<sub>2.5</sub> concentrations and other related variables, respectively, while  $\bar{x}$  and  $\bar{y}$  denote their mean values.

**Mann–Kendall test:** The Mann–Kendall test, a non-parametric statistical tool, is utilized in this study for trend analysis in data series [60]. This method is apt for identifying monotonic trends, either increasing or decreasing, in time series data without necessitating a specific data distribution. This study employed the  $p$ -values from the Mann–Kendall test to ascertain the trend in the contribution of IHS-related PM<sub>2.5</sub> concentrations. It provides both the slope of the contribution change and its 95% confidence interval. A trend is deemed significant if the  $p$ -value is below 0.05. Additionally, a  $z$ -value above 0 indicates an upward trend, whereas a  $z$ -value below 0 indicates a downward trend.

**Spatial autocorrelation analysis:** Spatial autocorrelation analysis is a statistical approach used to evaluate whether the spatial distribution of a variable shows systematic clustering or scattering [61]. This study applied spatial autocorrelation analysis to determine the spatial distribution patterns of IHS-related PM<sub>2.5</sub> concentrations. Typically, Moran’s I index is employed for this analysis, serving as an indicator of spatial correlation. Moran’s I index ranges from  $-1$  to  $+1$ , with values near  $+1$  indicating positive spatial correlation (clustering), those closer to  $-1$  suggesting negative correlation (dispersion), and values around 0 implying a random distribution. The Moran’s I index calculation is as follows:

$$I = \frac{n \sum_{i=1}^n \sum_{j=1}^n \omega_{ij} (x_i - \bar{x})(x_j - \bar{x})}{\sum_{i=1}^n \sum_{j=1}^n \omega_{ij} \sum_{i=1}^n (x_i - \bar{x})^2} \quad (13)$$

where  $n$  represents the number of pixels,  $x_i$  and  $x_j$  denote the IHS-related PM<sub>2.5</sub> concentration values at locations  $i$  and  $j$ ,  $\bar{x}$  is the average of all concentration values, and  $\omega_{ij}$  is the spatial weight between locations  $i$  and  $j$ .

### 3. Results

#### 3.1. Overall Spatial and Temporal Trends of PM<sub>2.5</sub> in the BTH Region

##### 3.1.1. Distribution and Variation of PM<sub>2.5</sub> Concentrations in the BTH Region

Figure 6 illustrates the spatial and temporal distribution of PM<sub>2.5</sub> concentrations throughout the BTH region. From 2012 to 2021, the area displayed a spatial pattern of higher concentrations in the southern parts and lower in the northern regions. The mean concentration per pixel varied between 26.89  $\mu\text{g}/\text{m}^3$  and 93.28  $\mu\text{g}/\text{m}^3$ , with an overall average of 54.96  $\mu\text{g}/\text{m}^3$ , as depicted in Figure 6a. Spatial analysis revealed that the average PM<sub>2.5</sub> concentration in IHS radiation areas was 84.90  $\mu\text{g}/\text{m}^3$ , reaching a peak of 281.74  $\mu\text{g}/\text{m}^3$  and a standard deviation of 39.84  $\mu\text{g}/\text{m}^3$ . Conversely, the background areas showed an average PM<sub>2.5</sub> concentration of 21.97  $\mu\text{g}/\text{m}^3$ , characterized by lower variability (standard deviation of 18.41  $\mu\text{g}/\text{m}^3$ ) and a peak concentration of 145.61  $\mu\text{g}/\text{m}^3$ , with less frequent occurrences of high concentration levels compared to the IHS radiation areas, as shown in Figure 6b. Statistical analysis using the Mann–Whitney U test indicated a significant difference ( $p < 0.01$ ) in the average PM<sub>2.5</sub> concentrations between IHS radiation and background areas, indicating a discernible impact of IHS operations on PM<sub>2.5</sub> concentrations.

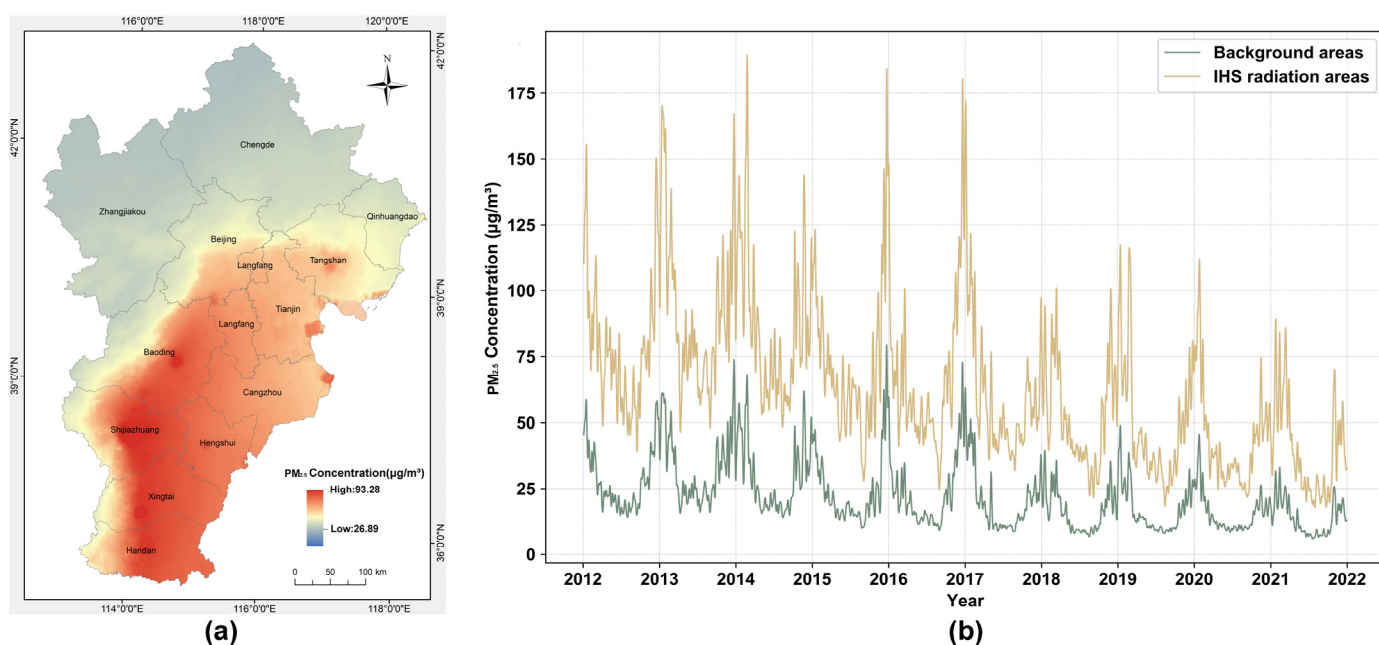


**Figure 6.** The spatial and temporal distribution of PM<sub>2.5</sub> concentrations in the BTH region from 2012 to 2021. (a) Spatial distribution of average PM<sub>2.5</sub> concentrations between 2012 and 2021. (b) Temporal distribution during 2012 and 2021 on background areas and IHS radiation areas.

##### 3.1.2. Analysis of IHS-Related PM<sub>2.5</sub> Concentrations and Influencing Factors in the BTH Region

Figure 7 displays the spatial and temporal distribution of IHS-related PM<sub>2.5</sub> concentrations and background concentrations, along with the factors influencing and the extent of the contributions of IHS-related PM<sub>2.5</sub>. The background concentration, influenced by meteorological and other anthropogenic factors, varied between  $-3.92 \mu\text{g}/\text{m}^3$  and 85.36  $\mu\text{g}/\text{m}^3$  with an average of 55.63  $\mu\text{g}/\text{m}^3$  in the BTH area from 2012 to 2021, as shown in Figure 7a. Excluding the background concentration, the IHS-related PM<sub>2.5</sub> concentration in radiation areas averaged 29.27  $\mu\text{g}/\text{m}^3$  (Figure 7b). Correlational analysis, considering the annual operational status of IHS, revealed a correlation coefficient of 0.94, highlighting a significant link between IHS operations and PM<sub>2.5</sub> levels (Figure 7c). When combining background and IHS contributions, approximately 33.16% of the total PM<sub>2.5</sub> concentration in these areas was attributed to IHSs (Figure 7d). Further, a Mann–Kendall trend analysis

of the contributions of IHS-related  $PM_{2.5}$  indicated a decreasing trend over time ( $p < 0.05$ ), signifying a year-over-year reduction in the influence of IHS production activities on  $PM_{2.5}$  concentrations and indicating some success in industrial reform efforts.

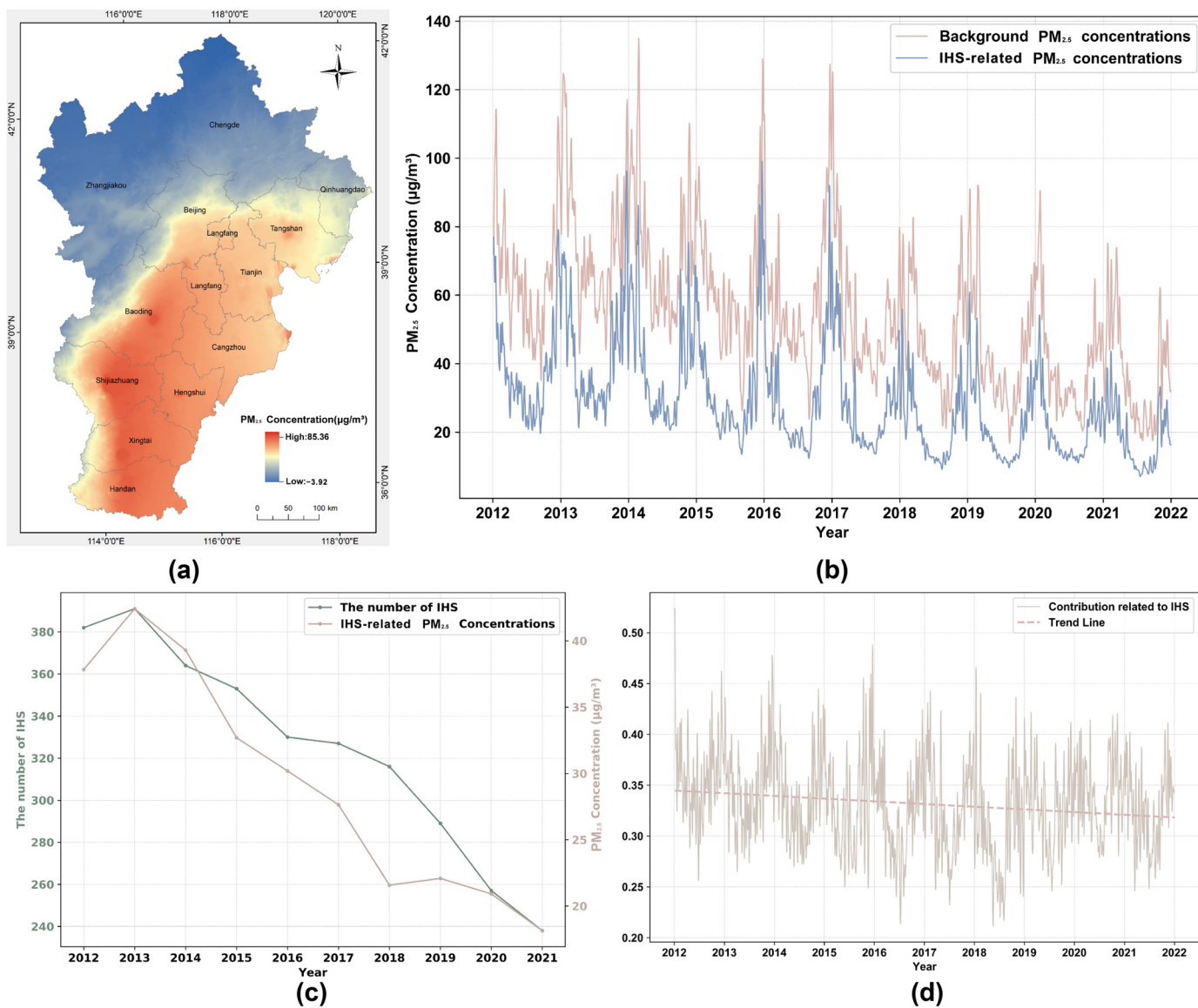


**Figure 7.** The spatial and temporal distribution of IHS-related  $PM_{2.5}$  concentrations and background concentrations in the BTH region from 2012 to 2021. (a) The average  $PM_{2.5}$  background concentration in the BTH region. (b) The temporal distribution of IHS-related  $PM_{2.5}$  concentrations and background concentrations. (c) Correlation of the number of IHSs and IHS-related  $PM_{2.5}$  concentrations on different years. (d)  $PM_{2.5}$  contribution related to IHS.

### 3.2. Analysis of the Spatial and Temporal Variations on IHS-Related $PM_{2.5}$ Concentrations in the BTH Region

#### 3.2.1. Temporal Trends and Seasonal Fluctuations on IHS-Related $PM_{2.5}$ Concentrations

The BTH region experienced considerable variability and a degree of periodicity in overall IHS-related  $PM_{2.5}$  concentrations from 2012 to 2021 (Figure 8a). The Mann–Kendall trend test indicated a declining trend in the annual mean IHS-related  $PM_{2.5}$  concentrations ( $S = -0.007, p < 0.05$ ), signifying statistical significance.

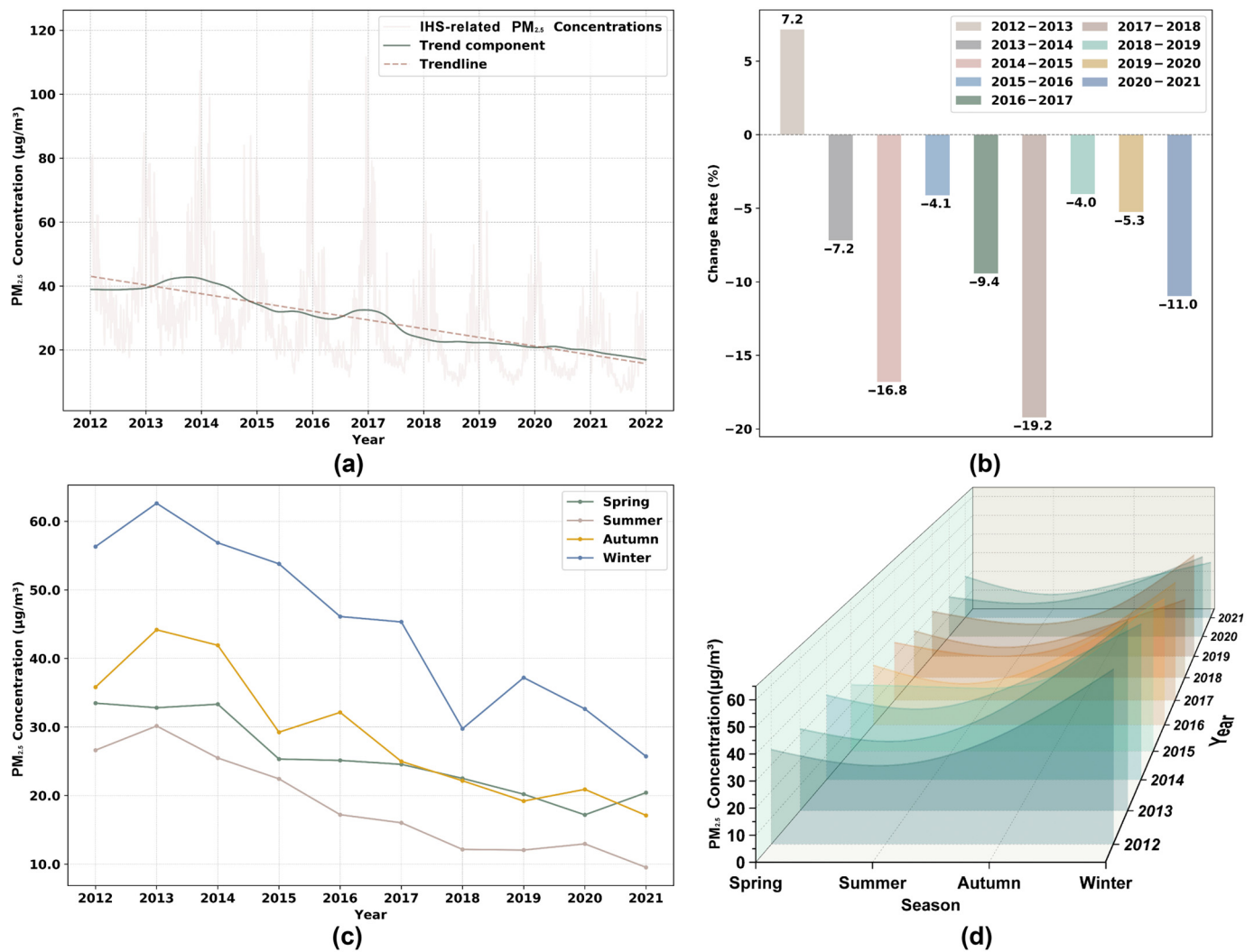


**Figure 8.** Temporal variations in IHS-related PM<sub>2.5</sub> concentrations in the BTH region during 2012 and 2021. (a) Temporal trends of IHS-related PM<sub>2.5</sub> concentrations from 2012 to 2021. (b) Rates of change in IHS-related PM<sub>2.5</sub> concentrations over two adjacent years. (c) Seasonal interannual variability of IHS-related PM<sub>2.5</sub> concentrations. (d) Seasonal trends in IHS-related PM<sub>2.5</sub> concentrations.

Regarding yearly variations, the peak average concentration occurred in 2013 at 42.42 µg/m<sup>3</sup>, while the lowest was recorded in 2021 at 18.14 µg/m<sup>3</sup>. The average concentration represented a 52.05% reduction from 2012 to 2021. Notably, there was a 7.2% increase in IHS-related PM<sub>2.5</sub> concentrations from 2012 to 2013. However, from 2014 to 2021, a continual decrease was observed, particularly in 2014–2015 and 2017–2018, with reductions of 16.8% and 19.2%, respectively, as shown in Figure 8b. These declines correlated with enforcing the Air Pollution Prevention and Control Action Plan and subsequent supply-side reforms. Post-2018, a continued decrease in IHS-related PM<sub>2.5</sub> concentrations was observed, with an increasing annual reduction rate, culminating in an 11.6% decrease in 2021 compared to 2020, following the dual-carbon policy implementation.

From 2012 to 2021, seasonal variations in IHS-related PM<sub>2.5</sub> concentrations in the BTH region showed a distinct pattern (Figure 8c). The trend displayed a ‘low in spring-summer and high in autumn-winter’ pattern, with winter concentrations being the highest, followed by autumn, spring, and summer. Spring concentrations averaged 25.50 µg/m<sup>3</sup>, summer at 18.46 µg/m<sup>3</sup>, autumn at 28.77 µg/m<sup>3</sup>, and winter at 44.64 µg/m<sup>3</sup>. Compared to 2012, each season in 2021 showed improvements, with varying degrees of reduction (Figure 8d). Summer saw the most significant decrease at 64.20%, an annual average

reduction of  $1.89 \mu\text{g}/\text{m}^3$ , followed by winter at 54.33% ( $3.40 \mu\text{g}/\text{m}^3$  annually), autumn at 52.23% ( $2.07 \mu\text{g}/\text{m}^3$  annually), and spring with the most minor decrease at 39.01% ( $1.45 \mu\text{g}/\text{m}^3$  annually). In particular after 2014, reductions were noted in each season, potentially reflecting the impact of regional environmental policies.

### 3.2.2. Spatial Distribution and Analysis of IHS-Related $\text{PM}_{2.5}$ Concentrations

The spatial distribution of IHS-related  $\text{PM}_{2.5}$  concentrations partially mirrors the industrial structure and the efficacy of environmental policies in distinct areas. Across the BTH region from 2012 to 2021, there was a consistent spatial trend of ‘lower in the north, higher in the south’ in IHS-related  $\text{PM}_{2.5}$  concentrations, with a stable distribution over the study period. The Moran’s I index for these concentrations stood at 0.98, reflecting a solid correlation with the density of industrial heat sources.

Notably, the pixel-level concentration map (Figure 9a) revealed that areas with the highest average  $\text{PM}_{2.5}$  values, mainly in Tangshan and Handan, showed peak concentrations up to  $78.40 \mu\text{g}/\text{m}^3$ . These areas were known for their dense industrial heat sources. In contrast, regions with fewer IHSs showed lower  $\text{PM}_{2.5}$  concentrations, indicative of reduced industrial emission densities. At the city level, the average IHS-related  $\text{PM}_{2.5}$  concentrations varied, not aligning with IHS density, which can be attributed to different industrial pollution control standards in each city (Figure 9b). Handan had the highest average concentration ( $37.60 \mu\text{g}/\text{m}^3$ ), followed by Cangzhou ( $37.45 \mu\text{g}/\text{m}^3$ ), with Zhangjiakou presenting the lowest ( $18.16 \mu\text{g}/\text{m}^3$ ). This pattern suggests that the southern parts of the BTH region are inclined towards industries with higher pollution and emissions, highlighting the need for more intensive industrial restructuring and enforcement of environmental regulations.

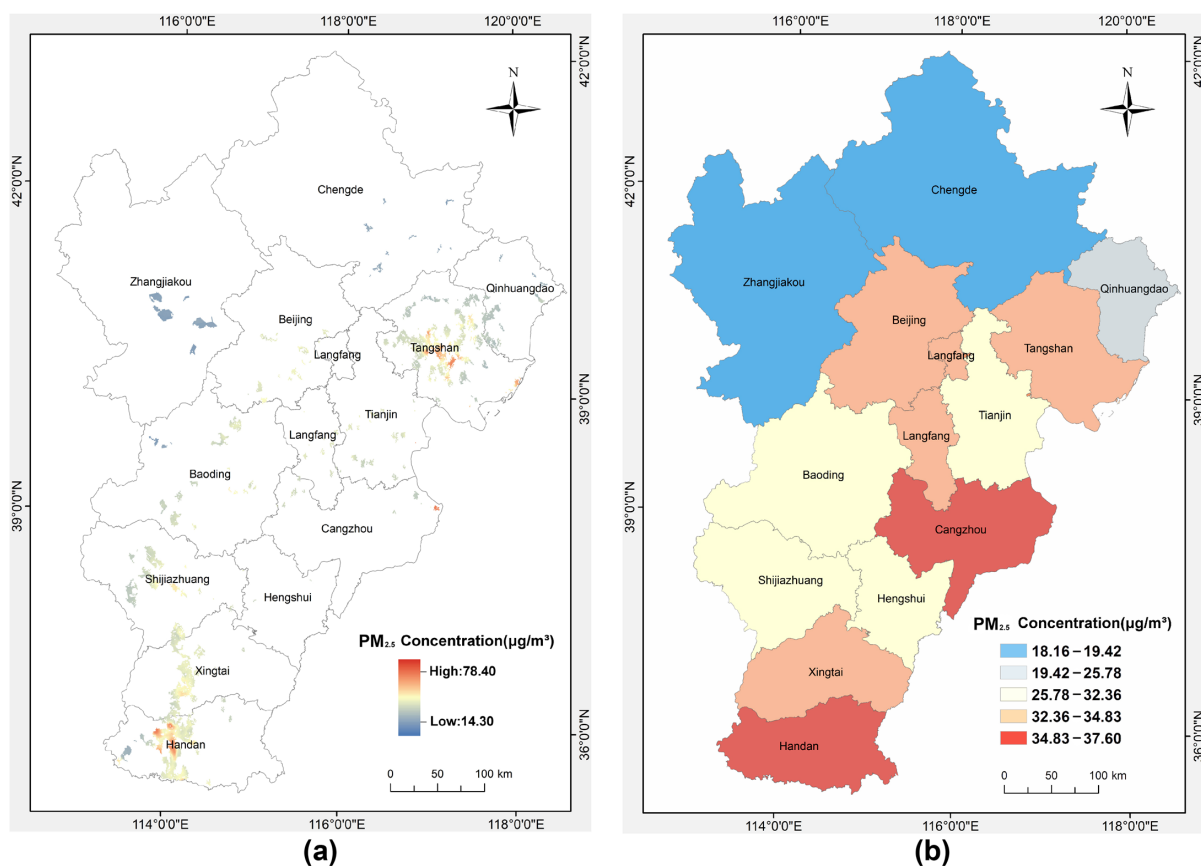


**Figure 9.** Spatial distribution of average IHS-related  $\text{PM}_{2.5}$  concentrations between 2012 and 2021. (a) The pixel-level average IHS-related  $\text{PM}_{2.5}$  concentrations. (b) The city-level average IHS-related  $\text{PM}_{2.5}$  concentrations.

### 3.2.3. Heterogeneity and Evolution of IHS-Related PM<sub>2.5</sub> Concentrations in the BTH

As Figure 10 and Table 2 illustrate, the spatial and temporal evolution of IHS-related PM<sub>2.5</sub> concentrations in the 13 cities of the BTH region exhibit notable heterogeneity. In 2012, concentrations varied from 14.33 μg/m<sup>3</sup> to 55.14 μg/m<sup>3</sup>, with contributions ranging between 26% and 55% (Figure 10a, Table 2). Regions with active IHS clusters, such as Cangzhou, Tangshan, Tianjin, and Handan, had noticeably higher concentrations and contributions than other areas. By 2021, all 13 cities significantly improved concentration levels and contribution rates of IHS-related PM<sub>2.5</sub> (Figure 10b). Concentrations ranged from 7.39 μg/m<sup>3</sup> to 23.83 μg/m<sup>3</sup>, with contributions between 22% and 46%. Between 2012 and 2021, the decrease in IHS-related PM<sub>2.5</sub> concentrations ranged from 36.09% to 57.23%, with Xingtai experiencing the most significant drop and Qinhuangdao the least (Table 2). Correspondingly, the decrease in contribution rates varied from 9.41% to 35.62%, with Tianjin showing the most substantial decline and Qinhuangdao the least.

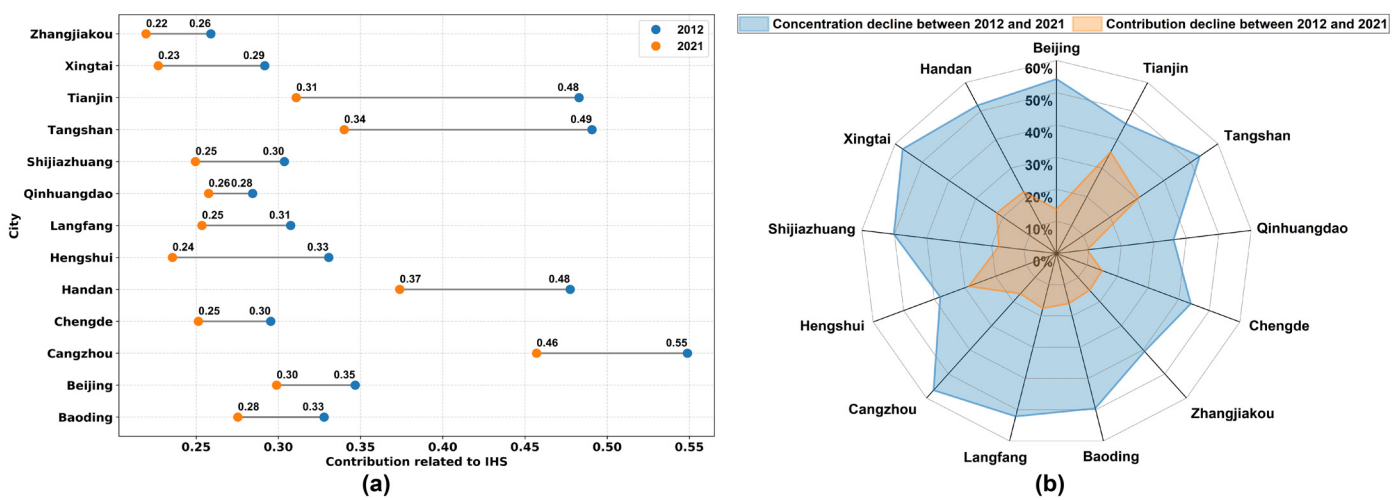


**Figure 10.** The contribution of IHS-related PM<sub>2.5</sub> concentrations in the BTH region. (a) The annual average contributions of IHS-related PM<sub>2.5</sub> in cities of the BTH region from 2012 to 2021. (b) Annual mean IHS-related PM<sub>2.5</sub> concentration and contribution rate changes in cities of the BTH region from 2012 to 2021.

**Table 2.** IHS-related PM<sub>2.5</sub> concentrations (μg/m<sup>3</sup>) in cities of the BTH region from 2012 to 2021.

	2012	2013	2014	2015	2016	2017	2018	2019	2020	2021	Decline between 2012 and 2021 (%)
Baoding	24.19	29.93	30.90	23.99	23.65	19.12	15.78	14.03	13.15	12.19	49.59%
Beijing	24.93	29.86	30.10	26.86	24.54	20.09	15.62	13.47	12.07	11.41	54.24%
Cangzhou	55.14	60.87	57.93	51.72	48.55	39.13	31.34	30.57	29.39	23.83	56.79%
Chengde	14.33	15.17	16.32	12.28	11.31	10.45	8.66	8.30	7.67	8.03	43.97%
Handan	42.86	44.59	42.61	37.63	33.12	32.13	24.12	27.59	25.50	20.57	52.00%
Hengshui	22.69	28.41	23.83	21.81	19.58	23.24	18.19	18.60	11.99	14.05	38.09%
Langfang	25.38	30.17	28.17	24.49	22.94	18.05	14.24	14.52	13.17	12.15	52.13%
Qinhuangdao	16.95	19.93	18.86	15.83	15.52	13.90	11.52	12.10	10.41	10.83	36.09%
Shijiazhuang	24.46	34.09	31.25	23.47	24.50	19.53	15.74	14.88	13.21	12.19	50.17%
Tangshan	41.08	44.52	38.24	31.34	28.54	27.30	20.88	21.94	20.68	19.19	53.29%
Tianjin	34.66	40.93	38.43	34.09	22.33	28.63	25.44	24.14	22.80	18.88	45.54%
Xingtai	26.91	37.40	33.30	24.76	22.53	18.34	15.01	14.77	12.15	11.51	57.23%
Zhangjiakou	12.44	12.76	12.93	10.95	9.98	9.82	8.68	7.21	6.98	7.39	40.61%

A variance analysis further determined the differences in IHS-related PM<sub>2.5</sub> concentrations among cities from 2012 to 2021 and the extent of fluctuations in each city. Figure 11 displays the distribution of IHS-related PM<sub>2.5</sub> concentrations across three critical years

(2012, 2017, and 2021) and over the decade. Generally, Cangzhou had the highest median concentration in all measured years, with a wide interquartile range (IQR), indicating substantial variability in IHS-related PM<sub>2.5</sub> concentrations. In contrast, Zhangjiakou exhibited the lowest median concentration and a narrow IQR, suggesting consistent pollution levels with fewer outliers (Figure 11d).

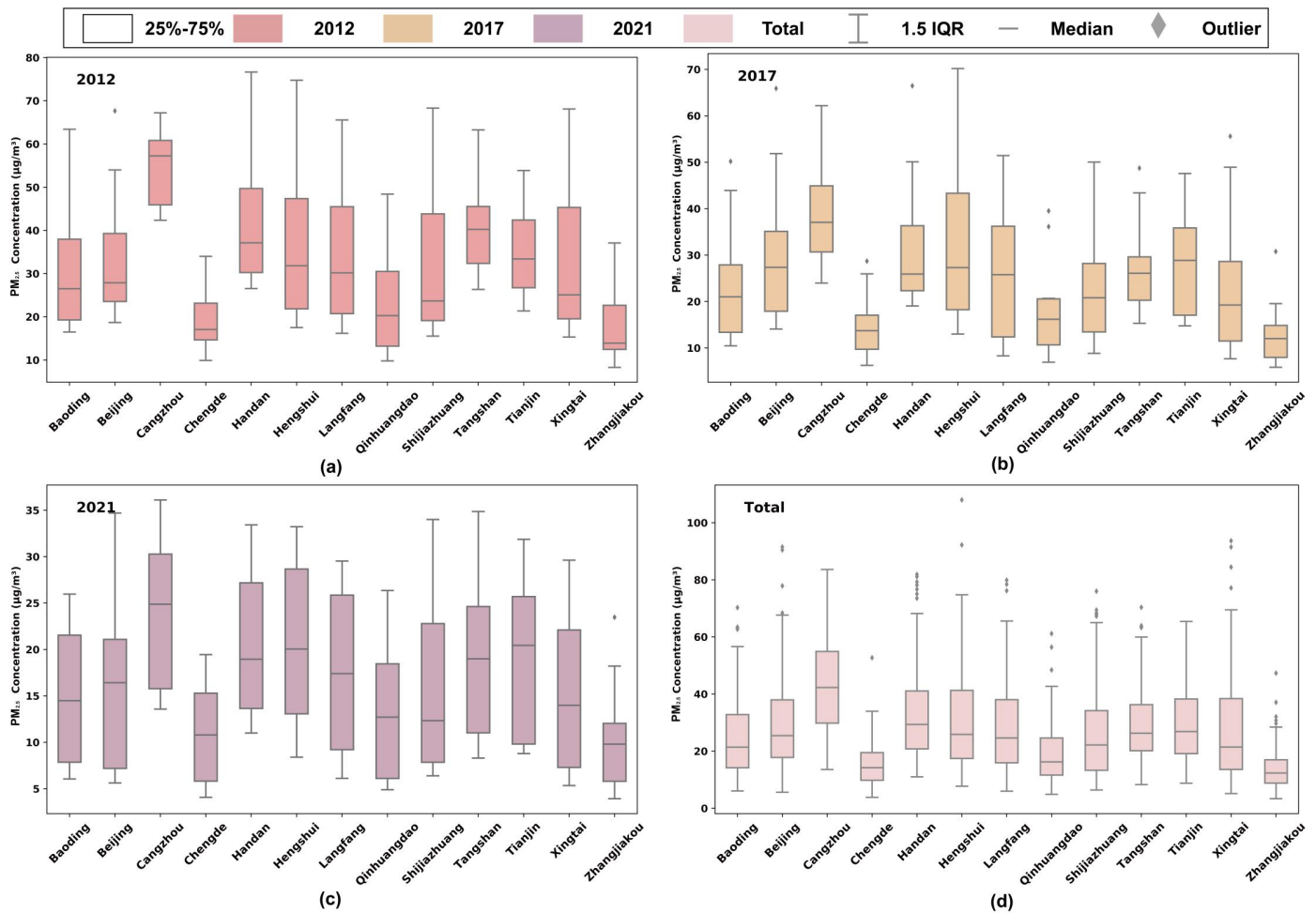


**Figure 11.** Box plots of IHS-related PM<sub>2.5</sub> concentrations in cities of the BTH region. (a) In 2012. (b) In 2017. (c) In 2021. (d) Ranging from 2012 to 2021.

In 2012, the median concentrations of IHS-related PM<sub>2.5</sub> in cities ranged from 13.91 µg/m<sup>3</sup> to 57.26 µg/m<sup>3</sup> (Figure 11a). Xingtai had the largest IQR (25.79 µg/m<sup>3</sup>), followed by Hengshui (25.52 µg/m<sup>3</sup>). Conversely, Chengde exhibited the most stable concentration levels, with an IQR of 8.51 µg/m<sup>3</sup>. By 2017, the median concentrations in all cities had noticeably decreased from 2012 levels, with Cangzhou and Tangshan experiencing the most significant reductions of 35.30% and 35.15%, respectively (Figure 11b). Cities like Baoding, Handan, Qinhuangdao, Shijiazhuang, Tangshan, Xingtai, and Zhangjiakou saw a significant reduction in IQR fluctuations, with Shijiazhuang’s reduction being particularly pronounced, dropping from 24.72 µg/m<sup>3</sup> in 2012 to 14.74 µg/m<sup>3</sup> in 2017. Meanwhile, fluctuations in Beijing and Tianjin slightly increased, with Tianjin experiencing the largest increase of 19.19%. Other regions maintained relatively stable IQR fluctuations. By 2021, the median concentrations of IHS-related PM<sub>2.5</sub> in cities continued to decline (Figure 11c). Shijiazhuang and Beijing saw the largest decreases, with reductions of 40.74% and 39.98%, respectively. Cities like Baoding, Beijing, Hengshui, Langfang, Tianjin, Xingtai, and others experienced significant reductions in IQR fluctuations, with Hengshui showing the most notable decrease, dropping from 25.09 µg/m<sup>3</sup> in 2017 to 15.60 µg/m<sup>3</sup> in 2021. Chengde, Qinhuangdao,

and Tangshan saw slight increases in IQR fluctuations, with Tangshan having the largest increase of 31.32%. Other areas maintained relatively stable IQR fluctuations.

The observations from 2012, 2017, and 2021, as well as the average over the decade, were consistent, indicating a gradual improvement, although not uniform, in the impact of IHSs on air pollution. There were significant disparities both within and between cities, necessitating continued attention to fine-tuning and implementing localized industrial emission reduction strategies.

### 3.3. Analysis of IHS-Related $PM_{2.5}$ Concentrations Focusing on Typical IHS

In the southwest of She County in Handan ( $113^{\circ}35'00''$  E– $113^{\circ}42'00''$  E,  $36^{\circ}28'00''$  N– $36^{\circ}35'00''$  N), the IHS radiation area included two adjacent IHSs: Jinyu Cement Factory and Xilin Technology Company (Figure 12a). While Jinyu Cement Factory has been continuously operational, Xilin Technology commenced operations in 2017. From 2012 to 2021, the IHS-related  $PM_{2.5}$  concentration in this industrial area fluctuated with an average concentration of  $19.20 \mu\text{g}/\text{m}^3$ . A clear peak in IHS-related  $PM_{2.5}$  concentration occurred in 2013 (Figure 12b). Despite these short-term fluctuations, a declining trend was evident ( $S = -0.005$ ,  $p < 0.05$ ), signifying the effectiveness of long-term emission reduction initiatives.

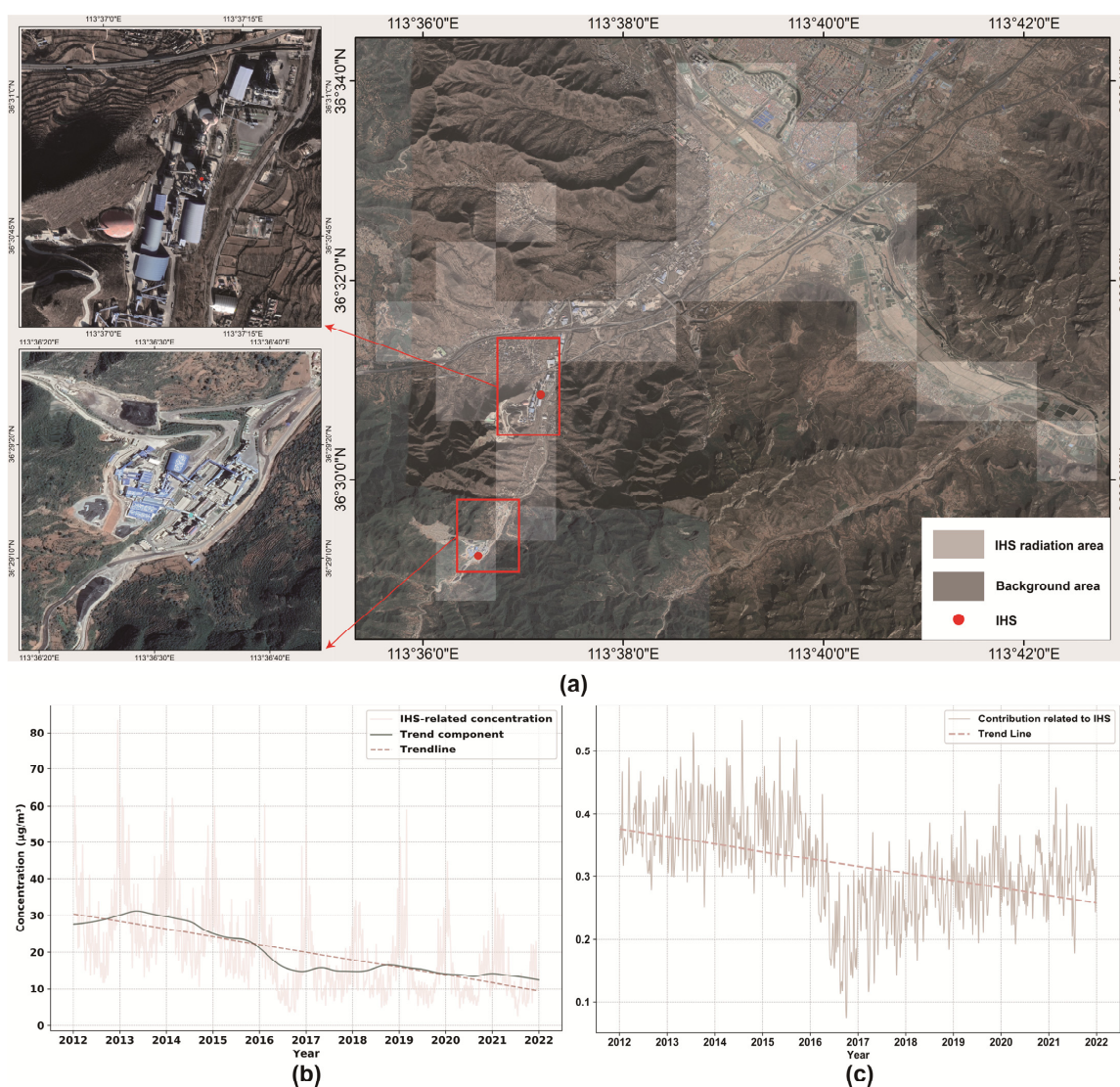


**Figure 12.** Analysis of IHS-related  $PM_{2.5}$  concentrations focusing on southwest of She county in Handan. (a) The location of IHS radiation area. (b) Temporal trends of IHS-related  $PM_{2.5}$  concentrations from 2012 to 2021. (c)  $PM_{2.5}$  contribution related to IHSs.

The annual IHS-related  $PM_{2.5}$  concentration in this IHS radiation area varied. From 2012 to 2013, there was an uptrend with an average increase of 7.48%. Post the launch of the 'Air Pollution Prevention and Control Action Plan' in 2013, a consistent decline in concentrations was observed from 2013 to 2016, with the rate of decrease growing each year: 7.38%, 15.93%, and 34.12%, respectively. With Xilin Technology commencing in 2017, the area's industrial heat source count rose to two. Between 2016 and 2019, the annual mean IHS-related  $PM_{2.5}$  concentration showed limited fluctuations. Impacted by the COVID-19 pandemic and the dual-carbon policy, a reduction of 13.79% in IHS-related  $PM_{2.5}$  concentration occurred in 2020 compared to 2019, with a continued decrease of 1.86% in 2021.

As shown in Figure 12c, the daily contributions of IHS-related  $PM_{2.5}$  concentrations ranged from 7.61% to 55.06% between 2012 and 2021. The trend line indicated an overall decrease in contribution rates, with the annual average contribution in 2021 being 29.21%, a decrease of 8.39% from 37.60% in 2012. Notably, during a partial shutdown of Jinyu Cement Factory from November 2016 to March 2017, the contribution rate of IHS-related  $PM_{2.5}$  fell to merely 20.95%, a substantial decline of 14.94% compared to the same period in the previous year. In sum, this observed temporal decrease and consistent industrial contributions highlight the importance of continuous monitoring of industrial emissions.

## 4. Discussion

### 4.1. Interrelations of Factors Affecting IHS-Related $PM_{2.5}$ Concentrations

Table 3 elucidates the intricate dynamics between IHS-related  $PM_{2.5}$  concentrations and various indicators signaling industrial activity, energy usage, and environmental emissions. Predominantly, metrics associated with operational IHSs, industrial indices, and environmental emissions showcased a strong positive correlation with IHS-related  $PM_{2.5}$  concentrations; however, specific raw material production correlations were less pronounced. Specifically,

- (1) The quantity of operational IHSs across the three provinces exhibited a potent positive correlation with IHS-related  $PM_{2.5}$  concentrations. Considering the direct emission of particulates from these IHSs during production processes, the number and active status of these IHSs have been identified as significant factors influencing ambient  $PM_{2.5}$  concentrations.
- (2) Metrics like energy consumption level, industry scale, and secondary sector gross domestic product (GDP) were highly correlated with IHS-related  $PM_{2.5}$  concentrations, especially in Hebei (0.93, 0.88, and 0.95, respectively). This implied that the existence of IHSs and their operational magnitudes substantially impact air quality. Significantly, regional differences were evident in the correlations between IHS-related  $PM_{2.5}$  concentrations and industrial indices. Industry scale in Tianjin and secondary sector GDP in Beijing with IHS-related  $PM_{2.5}$  concentrations were relatively modest. This pattern indicated that higher economic output was not necessarily synonymous with increased pollution levels, potentially signifying a shift in the economic composition of these regions towards cleaner technologies and services.
- (3) The correlations between raw material production and IHS-related  $PM_{2.5}$  concentrations exhibited notable variations. These differences suggested that distinct production processes, varying degrees of technological adoption, and the effectiveness of pollution control measures significantly impact  $PM_{2.5}$  emissions. Steel and cement production in Beijing and Tianjin moderately correlated with IHS-related  $PM_{2.5}$  concentrations, indicating contributions to particulate levels, yet subject to policy-induced production moderation and response adjustments. The exceedingly high correlation with raw coal production (0.98) in Hebei signaled the region's historical dependence on coal and high-polluting industrial processes. Also, it highlighted the province's pace of coal industry reform, directly affecting  $PM_{2.5}$  levels. Conversely, the negative correlation with steel production (−0.86) reflected a transition to modernized steel production technologies, ensuring environmental cleanliness while boosting production efficiency.

- (4) SO<sub>2</sub> and NO<sub>x</sub> emissions across all three provinces were strongly correlated with IHS-related PM<sub>2.5</sub> concentrations, notably at 0.94 for SO<sub>2</sub> and 0.93 for NO<sub>x</sub> in Hebei. These correlations highlight the need for improved combustion efficiency and better desulfurization and denitrification processes. Additionally, transitioning to cleaner energy sources is essential for substantially reducing PM<sub>2.5</sub> levels. The high correlation between industrial wastewater discharges and carbon emissions reflects broader environmental management practices within industries. Adequate wastewater treatment and low-carbon energy sources reduce IHS-related PM<sub>2.5</sub> concentrations.

**Table 3.** Correlation coefficients between IHS-related PM<sub>2.5</sub> concentrations and associated indicators.

Associated Indicators		Beijing	Tianjin	Hebei
IHS	Operational IHSs	0.94	0.82	0.92
	Energy consumption level	0.82	0.79	0.93
Industrial indices	Industry scale	0.89	0.69	0.88
	Secondary sector GDP	0.80	0.92	0.95
	Raw coal production	NAN <sup>1</sup>	NAN	0.98
Raw material production	Steel production	0.21	0.35	−0.86
	Gas production	−0.24	−0.83	0.95
	Cement production	0.82	0.75	0.29
	SO <sub>2</sub> emissions	0.72	0.50	0.94
Environmental emissions	NO <sub>x</sub> emissions	0.89	0.91	0.93
	Industrial wastewater discharges	0.86	0.83	NAN
	Industrial energy carbon emissions		0.86	

<sup>1</sup> NAN indicates missing statistics.

In a word, the correlation between economic activities, industrial practices, and environmental emissions profoundly influenced IHS-related PM<sub>2.5</sub> concentration levels. The above correlations between IHS-related PM<sub>2.5</sub> concentrations and industrial activities highlighted the necessity for stricter emission controls and cleaner production processes. Furthermore, the sustained strong correlations also illustrated the environmental latency in response to industrial practices and policy changes, underscoring the necessity for continuous policy assessment and refinement.

#### 4.2. Comparison with Other Previous Studies

The previous literature has predominantly focused on industry-specific source apportionment of PM<sub>2.5</sub>. However, these studies have varied in their methods of industrial categorization and analytical models. IHSs typically include cement and steel plants, oil refineries and exploration fields, chemical processing plants, and power generation facilities [48]. Wang, Li, and Wang utilized different numerical simulation models—RegAEM-APSA, CAMx, and CMAQ—for the source apportionment of PM<sub>2.5</sub> in the BTH region during January and February 2013 [62–64]. Their results in industrial source decomposition were comparable to the IHS-related PM<sub>2.5</sub> concentrations in this study (Table 4). The contribution rates of IHS-related PM<sub>2.5</sub> concentrations in our study were observed aligning with the industrial proportions reported in these previous studies. However, our study reported higher proportions in certain regions, possibly due to variations in classification criteria and regional delineations. IHS-related concentrations in our study, including contributions from some power plants and combustion sources, did not entirely match the industrial categories in atmospheric simulation methods. Furthermore, this study concentrated on IHS radiation areas, inherently exhibiting higher average PM<sub>2.5</sub> levels than the broader regional analysis in source apportionment methods. Liu used an emissions inventory and extensions-particulate matter source apportionment technology (PSAT) for decomposing PM<sub>2.5</sub> levels in Beijing in July 2012 [27]. Their categorization of steel mills, cement plants, and power plants can be compared with the IHSs in this study. The findings showed that the contribution sources in this study were slightly lower than those in Liu (Table 4). This

could be due to the classification of oil and gas development and coal chemical-related IHS contributions under other industrial sectors in Liu's analysis.

**Table 4.** Comparison of the contribution of this study with previous studies of IHS-related PM<sub>2.5</sub> concentration.

Date	Region	This Study	Similar Studies	Reference
2013.1–2013.2	Shijiazhuang	35.79%	37.00%	Li (2015) [63]
			36.20%	Wang (2014) [62]
	Xingtai	36.26%	29.20%	Wang (2020) [64]
			30.00%	Li (2015) [63]
2012.7	Beijing	22.55%	34%	Wang (2014) [62]
			32%	Wang (2020) [64]
			24%	Liu (2020) [27]

Compared with earlier studies, the contribution rates of IHS-related PM<sub>2.5</sub> concentrations in our research on an urban scale align well with source apportionment methodologies for the same period. However, the literature has yet to offer a similar analysis for specific IHS areas, thus limiting direct comparisons. This study's advantages over previous research include:

- (1) **Long Time Series with High Temporal Resolution:** Unlike past studies that have mainly analyzed PM<sub>2.5</sub> compositions over shorter monthly periods, our study provided a long-term daily time series of IHS-related PM<sub>2.5</sub> concentrations. This supported the identification of daily anomalies and long-term trends in industrial production.
- (2) **Focus on individual IHS targets:** In advancing past the methodologies of the previous research that have predominantly utilized regional emission inventories, this study uniquely pinpointed the exact locations of each IHS. This precision facilitated a more granular analysis of the specific impact exerted by individual IHS units on PM<sub>2.5</sub> concentrations. Constructing a 1 km × 1 km resolution radiation area around each IHS accurately extracted IHS-related PM<sub>2.5</sub> concentrations for the impacted areas, providing a scientific basis for assessing the specific impact of factories on air quality.
- (3) **Model Portability and Computational Efficiency:** The model employed in this study not only demonstrated computational efficiency but also offered adaptability across different industrial and geographical contexts. This versatility enhanced the model's applicability in varied environmental research scenarios.

#### 4.3. Significance and Uncertainties of the Study

This study extracted IHS-related PM<sub>2.5</sub> concentrations in the BTH region from 2012 to 2021 and analyzed their spatial and temporal trends and influencing factors. These findings are crucial for comprehending the dynamics of regional air pollution and the impact of industrial emissions on the environment. This study effectively separated PM<sub>2.5</sub> concentrations influenced by IHSs through the exclusion of meteorological and other non-industrial factors, offering a relatively precise delineation of industrial air pollution. Notably, this research pioneered a model tailored for extracting IHS-related PM<sub>2.5</sub> concentrations, enabling monitoring of the impact of individual IHSs on air quality. These innovative approaches have enriched the methods and theories for assessing the effectiveness of industrial air pollution control policies, providing valuable data and analytical tools for atmospheric policy evaluation. Furthermore, the outcomes offer vital scientific insights for developing and optimizing air quality management strategies, enhancing regional environmental quality, and fostering sustainable industrial development.

Nevertheless, this research is characterized by inherent uncertainties. Limitations in data acquisition and processing could introduce errors in the models and analytical methods employed, such as in the quality of source data and the definition of IHS radiation areas. Potential biases in the CHAP dataset, such as varying calibration standards and satellite data discrepancies, could impact PM<sub>2.5</sub> concentration representation. Similarly, the

ERA5 dataset may have uncertainties influenced by urban heat islands and specific meteorological conditions in the BTH region, affecting temperature and precipitation accuracy. Moreover, while this study endeavored to isolate non-IHS-related PM<sub>2.5</sub> concentrations thoroughly, residues of influences from biomass combustion and vehicular emissions were only partially extricated. Additionally, the methodology cannot disaggregate specific PM<sub>2.5</sub> concentrations for each heat source in areas with multiple IHSs.

Future research should focus on refining methodologies to assess the impact of IHSs on air quality more accurately. A key area for further study involves effectively separating non-IHS-related PM concentrations, particularly those contributions from biomass burning and traffic emissions. This would likely entail integrating more diverse data types, such as traffic flow statistics and spatial distribution data of biomass burning activities, and considering using more complex statistical models and machine learning algorithms to enhance analytical precision.

## 5. Conclusions

This research developed a new three-stage model using multi-source long-term sequential data to estimate IHS-related PM<sub>2.5</sub> concentrations, focusing on the BTH region from 2012 to 2021. The new three-stage model based on region-growing, STL decomposition, multiple regression methods, and U-ConvLSTM algorithms can identify the IHS radiation areas and eliminate the influence of meteorological and anthropogenic factors on IHS-related PM<sub>2.5</sub> concentrations. Then, the daily IHS-related PM<sub>2.5</sub> concentrations in the BTH region were obtained. The key findings are as follows:

- (1) Within the study area, the average PM<sub>2.5</sub> concentrations in IHS radiation areas were significantly higher than in background areas, with approximately 33.16% of PM<sub>2.5</sub> concentration attributable to IHS activities. Furthermore, a year-over-year decline in the contribution of IHS-related PM<sub>2.5</sub> was observed, indicating the effectiveness of industrial reform measures.
- (2) The annual mean IHS-related PM<sub>2.5</sub> concentration in the BTH region exhibited a general downward trend with a 5.78% average annual reduction. Seasonal analysis revealed a pronounced “low in spring-summer, high in autumn-winter” pattern, with the highest concentrations in winter. Spatial distribution analysis showed that IHS-related PM<sub>2.5</sub> concentrations in the southern, industrially dense areas were significantly higher than in the north, and the 13 cities within the region displayed varied temporal and spatial trends in IHS-related PM<sub>2.5</sub> concentrations. These findings underscore the importance of industrial activities and regional environmental policies in air pollution control.
- (3) In the specific industrial area of She County, Handan, two IHSs contributed an average of 19.20 µg/m<sup>3</sup> to the IHS-related PM<sub>2.5</sub> concentration. From 2012 to 2021, these concentrations fluctuated dynamically, peaking in 2013 and notably decreasing during partial shutdowns of IHS operations. This highlights the significant impact of the operational status of IHSs on local air quality.

The results not only offer a novel perspective on regional air pollution dynamics and the environmental impact of industrial emissions on a regional scale but also demonstrate the value of the developed IHS-related PM<sub>2.5</sub> concentration extraction model. This model enables monitoring of air quality impacts from individual IHS perspectives, providing valuable scientific support for formulating and optimizing air quality management strategies. Future studies should focus on refining the separation of IHS-related PM<sub>2.5</sub> from other sources like biomass burning and traffic emissions, potentially employing advanced statistical models and diverse data integration for enhanced accuracy.

**Author Contributions:** Conceptualization, C.M. and Y.Z.; methodology, C.M., Y.Z. and X.S.; validation, X.S.; formal analysis, X.S. and P.Z.; investigation, X.S.; resources, X.S.; data curation, X.S.; writing—original draft preparation, X.S.; writing—review and editing, C.M., J.Y. and D.W.; visualization, X.S. and R.L.; supervision, C.M. and Y.Z.; project administration, C.M. and Y.Z.; funding acquisition, C.M. and D.W.; All authors have read and agreed to the published version of the manuscript.

**Funding:** This research was supported by the National Key R&D Program of China (No. 2022YFF0606402), the China–Pakistan Joint Research Center of Earth Sciences, CAS-HEC, Islamabad 45320, Pakistan, and the Youth Innovation Promotion Association of the Chinese Academy of Science under Grant 2021126.

**Institutional Review Board Statement:** Not applicable.

**Informed Consent Statement:** Not applicable.

**Data Availability Statement:** The data presented in this study are available on request from the corresponding author. The data are not publicly available due to corporate privacy reasons.

**Acknowledgments:** The authors thank the editors and the three anonymous reviewers for their valuable comments that have helped to improve our manuscript.

**Conflicts of Interest:** The authors declare no conflicts of interest.

## References

1. Pozo-Luyo, C.A.; Cruz-Duarte, J.M.; Amaya, I.; Ortiz-Bayliss, J.C. Forecasting PM<sub>2.5</sub> Concentration Levels Using Shallow Machine Learning Models on the Monterrey Metropolitan Area in Mexico. *Atmos. Pollut. Res.* **2023**, *14*, 101898. [[CrossRef](#)]
2. Xiang, X.; Shi, G.; Wu, X.; Yang, F. The Extraordinary Trend of the Spatial Distribution of PM<sub>2.5</sub> Concentration and Its Meteorological Causes in Sichuan Basin. *Atmosphere* **2022**, *13*, 853. [[CrossRef](#)]
3. Silva, R.A.; Adelman, Z.; Fry, M.M.; West, J.J. The Impact of Individual Anthropogenic Emissions Sectors on the Global Burden of Human Mortality Due to Ambient Air Pollution. *Environ. Health Perspect.* **2016**, *124*, 1776–1784. [[CrossRef](#)] [[PubMed](#)]
4. Rai, P.; Furger, M.; Slowik, J.G.; Zhong, H.; Tong, Y.; Wang, L.; Duan, J.; Gu, Y.; Qi, L.; Huang, R.-J.; et al. Characteristics and Sources of Hourly Elements in PM<sub>10</sub> and PM<sub>2.5</sub> during Wintertime in Beijing. *Environ. Pollut.* **2021**, *278*, 116865. [[CrossRef](#)]
5. Sharma, K.; Kumar, P.; Sharma, J.; Thapa, S.D.; Gupta, A.; Rajak, R.; Baruah, B.; Prakash, A.; Ranjan, R.K. Characterization of Polycyclic Aromatic Hydrocarbons (PAHs) Associated with Fine Aerosols in Ambient Atmosphere of High-Altitude Urban Environment in Sikkim Himalaya. *Sci. Total Environ.* **2023**, *870*, 161987. [[CrossRef](#)] [[PubMed](#)]
6. Nawaz, M.O.; Henze, D.K.; Anenberg, S.C.; Braun, C.; Miller, J.; Pronk, E. A Source Apportionment and Emission Scenario Assessment of PM<sub>2.5</sub>- and O<sub>3</sub>-Related Health Impacts in G20 Countries. *GeoHealth* **2023**, *7*, e2022GH000713. [[CrossRef](#)]
7. Xie, Z.; Li, Y.; Qin, Y. Allocation of Control Targets for PM<sub>2.5</sub> Concentration: An Empirical Study from Cities of Atmospheric Pollution Transmission Channel in the Beijing-Tianjin-Hebei District. *J. Clean. Prod.* **2020**, *270*, 122545. [[CrossRef](#)]
8. Zhu, Z.; Liao, H. Evaluation on the Effects of Joint Prevention and Control of Air Pollution in Beijing-Tianjin-Hebei Region and Its Surrounding Areas—An Empirical Study Based on Multi-period Difference-in-Difference Model. *J. China Univ. Geosci.* **2022**, *22*, 142–156. [[CrossRef](#)]
9. Lestari, P.; Arrohan, M.K.; Damayanti, S.; Klimont, Z. Emissions and Spatial Distribution of Air Pollutants from Anthropogenic Sources in Jakarta. *Atmos. Pollut. Res.* **2022**, *13*, 101521. [[CrossRef](#)]
10. Artíñano, B.; Salvador, P.; Alonso, D.G.; Querol, X.; Alastuey, A. Anthropogenic and Natural Influence on the PM<sub>10</sub> and PM<sub>2.5</sub> Aerosol in Madrid (Spain). Analysis of High Concentration Episodes. *Environ. Pollut.* **2003**, *125*, 453–465. [[CrossRef](#)]
11. Tessum, M.W.; Anenberg, S.C.; Chafe, Z.A.; Henze, D.K.; Kleiman, G.; Kheirbek, I.; Marshall, J.D.; Tessum, C.W. Sources of Ambient PM<sub>2.5</sub> Exposure in 96 Global Cities. *Atmos. Environ.* **2022**, *286*, 119234. [[CrossRef](#)] [[PubMed](#)]
12. Pan, C.M.; Zhu, X.; Wang, J.; Xiang, F.; Qiu, F.; Wan, P.J. Research Progress on Emission Inventory of Air Pollution Sources. *Environ. Sci. Surv.* **2020**, *39*, 72–78. [[CrossRef](#)]
13. Gupta, L.; Bansal, M.; Nandi, P.; Habib, G.; Sunder Raman, R. Source Apportionment and Potential Source Regions of Size-Resolved Particulate Matter at a Heavily Polluted Industrial City in the Indo-Gangetic Plain. *Atmos. Environ.* **2023**, *298*, 119614. [[CrossRef](#)]
14. Oh, S.-H.; Park, K.; Park, M.; Song, M.; Jang, K.-S.; Schauer, J.J.; Bae, G.-N.; Bae, M.-S. Comparison of the Sources and Oxidative Potential of PM<sub>2.5</sub> during Winter Time in Large Cities in China and South Korea. *Sci. Total Environ.* **2023**, *859*, 160369. [[CrossRef](#)]
15. Zhang, Q.; Xue, D.; Liu, X.; Gong, X.; Gao, H. Process Analysis of PM<sub>2.5</sub> Pollution Events in a Coastal City of China Using CMAQ. *J. Environ. Sci.* **2019**, *79*, 225–238. [[CrossRef](#)] [[PubMed](#)]
16. Mebust, M.R.; Eder, B.K.; Binkowski, F.S.; Roselle, S.J. Models-3 Community Multiscale Air Quality (CMAQ) Model Aerosol Component 2. Model Evaluation. *J. Geophys. Res. Atmos.* **2003**, *108*, 2001JD001410. [[CrossRef](#)]
17. Liu, D.R.; Lee, S.J.; Huang, Y.; Chiu, C.J. Air Pollution Forecasting Based on Attention-Based LSTM Neural Network and Ensemble Learning. *Expert Syst.* **2020**, *37*, e12511. [[CrossRef](#)]

18. Danesh, Y.M.; Kuang, Z.; Dimakopoulou, K.; Barratt, B.; Suel, E.; Amini, H.; Lyapustin, A.; Katsouyanni, K.; Schwartz, J. Predicting Fine Particulate Matter (PM<sub>2.5</sub>) in the Greater London Area: An Ensemble Approach using Machine Learning Methods. *Remote Sens.* **2020**, *12*, 914. [[CrossRef](#)]
19. López-Aparicio, S.; Guevara, M.; Thunis, P.; Cuvelier, K.; Tarrasón, L. Assessment of Discrepancies between Bottom-up and Regional Emission Inventories in Norwegian Urban Areas. *Atmos. Environ.* **2017**, *154*, 285–296. [[CrossRef](#)]
20. Zhou, J.B.; Wang, X.; Xiu, R.L.; Li, L.N. Comparative Analysis of Atmospheric Pollutant Inventory and Environmental Statistics. *Environ. Monit. China* **2021**, *37*, 83–88. [[CrossRef](#)]
21. Duan, W.J.; Lang, J.L.; Cheng, S.Y.; Jia, J.; Wang, X.Q. Air Pollutant Emission Inventory from Iron and Steel Industry in the Beijing-Tianjin-Hebei Region and Its Impact on PM<sub>2.5</sub>. *Environ. Sci.* **2018**, *39*, 1445–1454. [[CrossRef](#)]
22. An, J.; Huang, Y.; Huang, C.; Wang, X.; Yan, R.; Wang, Q.; Wang, H.; Jing, S.; Zhang, Y.; Liu, Y.; et al. Emission Inventory of Air Pollutants and Chemical Speciation for Specific Anthropogenic Sources Based on Local Measurements in the Yangtze River Delta Region, China. *Atmos. Chem. Phys.* **2021**, *21*, 2003–2025. [[CrossRef](#)]
23. Wang, L. *Research on the Source Apportionment and Regional Transport of Fine Particulate Matter in the Atmosphere of Changchun City*; Jilin University: Changchun, China, 2023.
24. Pino-Cortés, E.; Carrasco, S.; Acosta, J.; de Almeida Albuquerque, T.T.; Pedruzzi, R.; Díaz-Robles, L.A. An Evaluation of the Photochemical Air Quality Modeling Using CMAQ in the Industrial Area of Quintero-Puchuncavi-Concon, Chile. *Atmos. Pollut. Res.* **2022**, *13*, 101336. [[CrossRef](#)]
25. Mazzeo, A.; Zhong, J.; Hood, C.; Smith, S.; Stocker, J.; Cai, X.; Bloss, W.J. Modelling the Impact of National vs. Local Emission Reduction on PM<sub>2.5</sub> in the West Midlands, UK Using WRF-CMAQ. *Atmosphere* **2022**, *13*, 377. [[CrossRef](#)]
26. Dong, D.M.; Du, S.S.; Huang, Y.S.; Man, R.Q.; Yao, M.Y.; Du, R.H.; Liang, D.P.; Ning, Y. Pollution Characteristics and Source Apportionment of PM<sub>2.5</sub> in Winter and Spring in Changchun City. *J. Jilin Univ.* **2020**, *58*, 1278–1286. [[CrossRef](#)]
27. Liu, X.; Bai, X.; Tian, H.; Wang, K.; Hua, S.; Liu, H.; Liu, S.; Wu, B.; Wu, Y.; Liu, W.; et al. Fine Particulate Matter Pollution in North China: Seasonal-Spatial Variations, Source Apportionment, Sector and Regional Transport Contributions. *Environ. Res.* **2020**, *184*, 109368. [[CrossRef](#)]
28. Wang, S.; Ren, Y.; Xia, B. PM<sub>2.5</sub> and O<sub>3</sub> Concentration Estimation Based on Interpretable Machine Learning. *Atmos. Pollut. Res.* **2023**, *14*, 101866. [[CrossRef](#)]
29. Murray, N.L.; Holmes, H.A.; Liu, Y.; Chang, H.H. A Bayesian Ensemble Approach to Combine PM<sub>2.5</sub> Estimates from Statistical Models Using Satellite Imagery and Numerical Model Simulation. *Environ. Res.* **2019**, *178*, 108601. [[CrossRef](#)]
30. Yuen, K.K.F. Towards Multiple Regression Analyses for Relationships of Air Quality and Weather. *J. Adv. Inf. Technol.* **2017**, *8*, 135–140. [[CrossRef](#)]
31. Ding, J.; Dai, Q.; Fan, W.; Lu, M.; Zhang, Y.; Han, S.; Feng, Y. Impacts of Meteorology and Precursor Emission Change on O<sub>3</sub> Variation in Tianjin, China from 2015 to 2021. *J. Environ. Sci.* **2023**, *126*, 506–516. [[CrossRef](#)] [[PubMed](#)]
32. Wu, Y.; Lin, S.; Shi, K.; Ye, Z.; Fang, Y. Seasonal Prediction of Daily PM<sub>2.5</sub> Concentrations with Interpretable Machine Learning: A Case Study of Beijing, China. *Environ. Sci. Pollut. Res.* **2022**, *29*, 45821–45836. [[CrossRef](#)]
33. Xu, W.; Fu, F.; Zhang, Q.; Wang, L. A Deep Learning-Based Multi-Objective Optimization Model for PM<sub>2.5</sub> Prediction. *Int. J. Comput. Intell. Syst.* **2023**, *16*, 141. [[CrossRef](#)]
34. Li, X.; Peng, L.; Yao, X.; Cui, S.; Hu, Y.; You, C.; Chi, T. Long Short-Term Memory Neural Network for Air Pollutant Concentration Predictions: Method Development and Evaluation. *Environ. Pollut.* **2017**, *231*, 997–1004. [[CrossRef](#)]
35. Rawat, W.; Wang, Z. Deep Convolutional Neural Networks for Image Classification: A Comprehensive Review. *Neural Comput.* **2017**, *29*, 2352–2449. [[CrossRef](#)] [[PubMed](#)]
36. Huang, C.J.; Kuo, P.H. A Deep CNN-LSTM Model for Particulate Matter (PM<sub>2.5</sub>) Forecasting in Smart Cities. *Sensors* **2018**, *18*, 2220. [[CrossRef](#)] [[PubMed](#)]
37. Chattopadhyay, A.; Mustafa, M.; Hassanzadeh, P.; Bach, E.; Kashinath, K. Towards Physics-Inspired Data-Driven Weather Forecasting: Integrating Data Assimilation with a Deep Spatial-Transformer-Based U-NET in a Case Study with ERA5. *Geosci. Model Dev.* **2022**, *15*, 2221–2237. [[CrossRef](#)]
38. Ma, Y.; Wang, L.; Zhao, F. Study on PM<sub>2.5</sub> Concentration Prediction Method Based on CONVLSTM and U-Net. *Environ. Eng.* **2023**, *41*, 1300–1304.
39. Wei, J.; Li, Z.; Lyapustin, A.; Sun, L.; Peng, Y.; Xue, W.; Su, T.; Cribb, M. Reconstructing 1-Km-Resolution High-Quality PM<sub>2.5</sub> Data Records from 2000 to 2018 in China: Spatiotemporal Variations and Policy Implications. *Remote Sens. Environ.* **2021**, *252*, 112136. [[CrossRef](#)]
40. Wei, J.; Li, Z.; Cribb, M.; Huang, W.; Xue, W.; Sun, L.; Guo, J.; Peng, Y.; Li, J.; Lyapustin, A.; et al. Improved 1Km Resolution PM<sub>2.5</sub> Estimates across China Using Enhanced Space–Time Extremely Randomized Trees. *Atmos. Chem. Phys.* **2020**, *20*, 3273–3289. [[CrossRef](#)]
41. Wei, J.; Li, Z. *ChinaHighPM<sub>2.5</sub>: Big Data Seamless 1 km Ground-level PM<sub>2.5</sub> Dataset for China (2000–2021)*; National Tibetan Plateau/Third Pole Environment Data Center: Beijing, China, 2023. [[CrossRef](#)]
42. Liang, X.; Liu, Z.; Zhai, L.; Ji, L.; Feng, Y.; Sang, H. Spatial Terrestrial Carbon Emissions/Sequestrations Evolution Based on Ecological Network Analysis in Beijing-Tianjin-Hebei Urban Agglomeration. *Ecol. Eng.* **2023**, *189*, 106914. [[CrossRef](#)]

43. Xue, W.; Zhang, J.; Hu, X.; Yang, Z.; Wei, J. Hourly Seamless Surface O<sub>3</sub> Estimates by Integrating the Chemical Transport and Machine Learning Models in the Beijing-Tianjin-Hebei Region. *Int. J. Environ. Res. Public Health* **2022**, *19*, 8511. [[CrossRef](#)] [[PubMed](#)]
44. Liu, N.; Li, S.; Zhang, F. Multi-Scale Spatiotemporal Variations and Drivers of PM<sub>2.5</sub> in Beijing-Tianjin-Hebei from 2015 to 2020. *Atmosphere* **2022**, *13*, 1993. [[CrossRef](#)]
45. Qiao, Y.; Ji, D.; Shang, H.; Xu, J.; Xu, R.; Shi, C. The Fusion of ERA5 and MERRA-2 Atmospheric Temperature Profiles with Enhanced Spatial Resolution and Accuracy. *Remote Sens.* **2023**, *15*, 3592. [[CrossRef](#)]
46. Sun, X.; Zhao, T.; Bai, Y.; Kong, S.; Zheng, H.; Hu, W.; Ma, X.; Xiong, J. Meteorology Impact on PM<sub>2.5</sub> Change over a Receptor Region in the Regional Transport of Air Pollutants: Observational Study of Recent Emission Reductions in Central China. *Atmos. Chem. Phys.* **2022**, *22*, 3579–3593. [[CrossRef](#)]
47. Sinergise. *Copernicus Global Digital Elevation Model*; Open Topography: San Diego, CA, USA, 2021. [[CrossRef](#)]
48. Ma, C.; Yang, J.; Chen, F.; Ma, Y.; Liu, J.; Li, X.; Duan, J.; Guo, R. Assessing Heavy Industrial Heat Source Distribution in China Using Real-Time VIIRS Active Fire/Hotspot Data. *Sustainability* **2018**, *10*, 4419. [[CrossRef](#)]
49. Ma, C.; Sui, X.; Zeng, Y.; Yang, J.; Xie, Y.; Li, T.; Zhang, P. Classification of Industrial Heat Source Objects Based on Active Fire Point Density Segmentation and Spatial Topological Correlation Analysis in the Beijing–Tianjin–Hebei Region. *Sustainability* **2022**, *14*, 11228. [[CrossRef](#)]
50. Wang, M.; Chen, H.; Lei, M. Identifying Potentially Contaminated Areas with MaxEnt Model for Petrochemical Industry in China. *Environ. Sci. Pollut. Res.* **2022**, *29*, 54421–54431. [[CrossRef](#)]
51. Jiang, Y.; Guo, X.; Ye, Y.; Xu, Z.; Zhou, Y.; Xia, F.; Shi, Z. Spatiotemporal Assessment and Scenario Simulation of the Risk Potential of Industrial Sites at the Regional Scale. *Sci. Total Environ.* **2024**, *906*, 167537. [[CrossRef](#)]
52. The Recommended Method for Risk Assessment of Environmental Emergencies in Administrative Regions. Available online: [https://www.mee.gov.cn/gkml/hbb/bgt/201802/t20180206\\_430931.htm](https://www.mee.gov.cn/gkml/hbb/bgt/201802/t20180206_430931.htm) (accessed on 30 June 2023).
53. Wang, G.; Li, X.; Zhao, K.; Li, Y.; Sun, X. Quantifying the Spatio-Temporal Variations and Impacts of Factors on Vegetation Water Use Efficiency Using STL Decomposition and Geodetector Method. *Remote Sens.* **2022**, *14*, 5926. [[CrossRef](#)]
54. Trull, O.; García-Díaz, J.C.; Peiró-Signes, A. Multiple Seasonal STL Decomposition with Discrete-Interval Moving Seasonalities. *Appl. Math. Comput.* **2022**, *433*, 127398. [[CrossRef](#)]
55. Wang, S.; Gao, J.; Guo, L.; Nie, X.; Xiao, X. Meteorological Influences on Spatiotemporal Variation of PM<sub>2.5</sub> Concentrations in Atmospheric Pollution Transmission Channel Cities of the Beijing–Tianjin–Hebei Region, China. *Int. J. Environ. Res. Public Health* **2022**, *19*, 1607. [[CrossRef](#)] [[PubMed](#)]
56. Gong, S.; Zhang, L.; Liu, C.; Lu, S.; Pan, W.; Zhang, Y. Multi-Scale Analysis of the Impacts of Meteorology and Emissions on PM<sub>2.5</sub> and O<sub>3</sub> Trends at Various Regions in China from 2013 to 2020 2. Key Weather Elements and Emissions. *Sci. Total Environ.* **2022**, *824*, 153847. [[CrossRef](#)] [[PubMed](#)]
57. Jia, F.; Tan, J.; Lu, X.; Qian, J. Radar Timing Range–Doppler Spectral Target Detection Based on Attention ConvLSTM in Traffic Scenes. *Remote Sens.* **2023**, *15*, 4150. [[CrossRef](#)]
58. Hu, H.C.; Chen, L. Parametric Hypothesis Test of P-Norm Distribution. *J. Wuhan Univ.* **2021**, *67*, 173–178. [[CrossRef](#)]
59. Li, Y.Y.; Hu, C.R. *Experimental Design and Data Processing*; Chemical Industry Press: Beijing, China, 2017; pp. 104–107.
60. Gocic, M.; Trajkovic, S. Analysis of Changes in Meteorological Variables Using Mann-Kendall and Sen’s Slope Estimator Statistical Tests in Serbia. *Glob. Planet. Chang.* **2013**, *100*, 172–182. [[CrossRef](#)]
61. Song, C.; Yu, Q.; Jin, K. Forest Resource Quality and Human Activity Intensity Change and Spatial Autocorrelation Analysis in Yulin City, China. *Forests* **2023**, *14*, 1929. [[CrossRef](#)]
62. Wang, L.T.; Wei, Z.; Yang, J.; Zhang, Y.; Zhang, F.F.; Su, J.; Meng, C.C.; Zhang, Q. The 2013 Severe Haze over Southern Hebei, China: Model Evaluation, Source Apportionment, and Policy Implications. *Atmos. Chem. Phys.* **2014**, *14*, 3151–3173. [[CrossRef](#)]
63. Li, X.; Zhang, Q.; Zhang, Y.; Zheng, B.; Wang, K.; Chen, Y.; Wallington, T.J.; Han, W.; Shen, W.; Zhang, X.; et al. Source Contributions of Urban PM<sub>2.5</sub> in the Beijing–Tianjin–Hebei Region: Changes between 2006 and 2013 and Relative Impacts of Emissions and Meteorology. *Atmos. Environ.* **2015**, *123*, 229–239. [[CrossRef](#)]
64. Wang, S.E. *Study on Source Apportionment of Air Complex Pollution in “2+26” Cities Around Beijing–Tianjin–Hebei Region*; Nanjing University: Nanjing, China, 2020. [[CrossRef](#)]

**Disclaimer/Publisher’s Note:** The statements, opinions and data contained in all publications are solely those of the individual author(s) and contributor(s) and not of MDPI and/or the editor(s). MDPI and/or the editor(s) disclaim responsibility for any injury to people or property resulting from any ideas, methods, instructions or products referred to in the content.